nature aging

Resource

https://doi.org/10.1038/s43587-024-00598-z

Proteomics of mouse brain endothelium uncovers dysregulation of vesicular transport pathways during aging

Received: 8 December 2021

Accepted: 20 February 2024

Published online: 22 March 2024



Katalin Todorov-Völgyi (1,111). Judit González-Gallego (1,2,11), Stephan A. Müller (1,2,3,4), Nathalie Beaufort (1, Rainer Malik (1, Martina Schifferer (1,2,3,4)), Mihail Ivilinov Todorov (1,6,4), Dennis Crusius (1,5), Sophie Robinson (1,2,3,4), Andree Schmidt (1,4,4), Jakob Körbelin (1,5,6), Florence Bareyre (1,5,8,9), Ali Ertürk (1,5,6), Christian Haass (1,5,10), Mikael Simons (1,5,5), Dominik Paquet (1,5,6), Stefan F. Lichtenthaler (1,5,6), Martin Dichgans (1,5,5).

■ **Control of the control of the contr

Age-related decline in brain endothelial cell (BEC) function contributes critically to neurological disease. Comprehensive atlases of the BEC transcriptome have become available, but results from proteomic profiling are lacking. To gain insights into endothelial pathways affected by aging, we developed a magnetic-activated cell sorting-based mouse BEC enrichment protocol compatible with proteomics and resolved the profiles of protein abundance changes during aging. Unsupervised cluster analysis revealed a segregation of age-related protein dynamics with biological functions, including a downregulation of vesicle-mediated transport. We found a dysregulation of key regulators of endocytosis and receptor recycling (most prominently Arf6), macropinocytosis and lysosomal degradation. In gene deletion and overexpression experiments, Arf6 affected endocytosis pathways in endothelial cells. Our approach uncovered changes not picked up by transcriptomic studies, such as accumulation of vesicle cargo and receptor ligands, including Apoe. Proteomic analysis of BECs from Apoe-deficient mice revealed a signature of accelerated aging. Our findings provide a resource for analysing BEC function during aging.

The central nervous system requires a tightly controlled metabolic environment for proper neuronal functioning and information processing. This specific environment is maintained by the blood-brain barrier (BBB), which is centrally positioned within the neurovascular unit and

endowed with unique properties¹. Brain endothelial cells (BECs), key constituents of the BBB, display exquisitely low rates of transcellular vesicular transport (transcytosis) and specialized tight junctions that restrict paracellular diffusion, thus safeguarding BBB integrity². BECs

¹Institute for Stroke and Dementia Research (ISD), University Hospital, LMU Munich, Munich, Germany. ²Graduate School of Systemic Neuroscience (GSN), University Hospital, LMU Munich, Munich, Germany. ³German Center for Neurodegenerative Diseases (DZNE) Munich, Munich, Germany. ⁴Neuroproteomics, School of Medicine and Health, Klinikum rechts der Isar, Technical University of Munich, Munich, Germany. ⁵Munich Cluster for Systems Neurology (SyNergy), Munich, Germany. ⁶Institute for Tissue Engineering and Regenerative Medicine (iTERM), Helmholtz Zentrum München, Neuherberg, Germany. ⁷Department of Oncology, Hematology and Bone Marrow Transplantation with Section Pneumology, University Medical Center Hamburg-Eppendorf, Hamburg, Germany. ⁸Institute of Clinical Neuroimmunology, University Hospital, LMU Munich, Munich, Germany. ⁹Biomedical Center Munich (BMC), Faculty of Medicine, LMU Munich, Planegg-Martinsried, Germany. ¹⁰Division of Metabolic Biochemistry, Biomedical Center Munich (BMC), Faculty of Medicine, Ludwig-Maximilians-Universität München, Munich, Germany. ¹¹These authors contributed equally: Katalin Todorov-Völgyi, Judit González-Gallego. ⊠e-mail: katalin.voelgyi@med.uni-muenchen.de; martin.dichgans@med.uni-muenchen.de

further play critical roles in neurovascular coupling^{3,4}, brain metabolism⁵ and immune activation⁶ through interaction with other cells.

Age-related dysregulation of BECs causes vascular dysfunction, thus critically contributing to cerebrovascular and neurodegenerative diseases⁷⁻¹². Previous studies have shown a decline of various BEC-dependent functions during aging, including BBB integrity^{13,14}, neurovascular coupling¹⁵ and cerebral blood flow¹⁶. However, the molecular alterations driving this decline are insufficiently understood. Candidate factors that have emerged from previous work include an increase in oxidative and nitrosative stress^{17,18}, changes in telomere length resulting in cellular senescence¹⁹ and specific molecules, such as integrins^{20,21}, ApoE^{22,23} and Medin, an amyloidogenic peptide that accumulates in the vasculature with aging²⁴⁻²⁶.

Molecular profiling studies have greatly contributed to understanding the effects of aging on specific tissues or cell types²⁷⁻²⁹. Specifically, single-cell RNA sequencing (scRNA-seq) of mouse BECs, along with proteomics of whole brain microvasculature, has shown an age-dependent shift in BBB transcytosis from ligand-specific receptor-mediated transport to non-specific caveolar endocytosis³⁰. scRNA-seq studies further revealed zonation-dependent transcriptomic changes in aged BECs^{31,32} and an upregulation of innate immunity and oxidative stress response pathways in capillary BECs from old compared to young mice³¹.

Although developments in transcriptomic analyses have enabled cellular mapping at single-cell resolution 33 , analyses of the proteome are needed for better understanding of the molecular pathways implicated in cellular function and aging. First, correlations between mRNA levels and their corresponding protein levels are often poor (Pearson's r^2 0.3–0.4) $^{34-38}$, because post-transcriptional processes that control protein synthesis and degradation have a major influence on protein abundances. Second, transcriptomic analyses typically do not capture molecules that are bound to the cell surface or internalized, such as receptor ligands or cargo from phagocytotic vesicles, respectively. Third, proteins are closer to the biosynthetic output and cellular functions than mRNA; however, to our knowledge, results of BEC proteomic profiling are lacking.

In the present study, we developed a BEC enrichment protocol compatible with liquid chromatography coupled with tandem mass spectrometry (LC–MS/MS) to resolve the mouse BEC proteome and gain insights into protein abundance changes during healthy aging. Using a recently developed method for unsupervised clustering^{39–42}, we identified distinct patterns of age-related protein dynamics that segregated with biological functions and the subcellular localization (SL) of proteins. Here we provide insights into endothelial vesicular transport pathways and identify Arf6, a key regulator of endocytosis and receptor recycling, as a candidate factor mediating vesicular transport changes during aging. We further present evidence for an accelerating effect of Apoe deficiency on BEC aging as well as cell-autonomous effects of APOE in human endothelial cells.

Results

Proteomic analysis of mouse BECs during aging

To assess changes of the mouse BEC proteome during aging, we first developed a protocol for BEC enrichment compatible with LC–MS/MS (Fig. 1a). Cd31 labeling and magnetic-activated cell sorting (MACS) resulted in the enrichment of BECs expressing adherens (Pecam1 and Cdh5) and tight junction markers (Cldn5) (Fig. 1b). Isolated BECs from 3-month-old and 18-month-old animals displayed ultrastructural hallmarks of endothelial cells, including nuclei with heterochromatin and endothelial protrusions (Fig. 1b). LC–MS/MS on isolated BECs and full brain tissue (FT) preparations from 3-month-old mice followed by label-free quantification (LFQ) showed a massive enrichment of endothelial markers, including Nos3 (fold change (FC):1,684.5), Cdh5 (29.9) and Pecam1 (30.7) in BECs compared to FT (Fig. 1c and Supplementary Table 1). Notably, their protein levels in BECs were stable

between 3 months and 18 months. Among other cell markers, we found a prominent reduction of neuronal (Map2 – FC: 0.01) and glial (Gfap – FC: 0.28) markers, a moderate reduction of glial end-feet markers (Aqp4 – FC: 0.77) and some enrichment of pericyte (Anpep – FC: 4.82) marker proteins. This is consistent with the results of CD31-based enrichment protocols for single-cell sequencing 44 , showing that a small population of other vascular cell types remains with these protocols.

Proteomic analysis of isolated BECs from 3-month-old, 6-month-old, 12-month-old and 18-month-old mice captured a total of 4,137 proteins. Among them, 3,754 proteins were identified with two or more unique peptides, of which 2,516 proteins were quantified in three or more samples in all age groups. In total, 850 proteins showed significant changes in abundance during aging (ANOVA, P < 0.05) (Fig. 1d and Supplementary Table 2). A comparison with published mouse bulk BEC RNA-seq data⁴⁵ revealed 193 proteins and corresponding RNAs that were significantly altered in both datasets (Fig. 1e). Notably, there was a weak but significant correlation ($r^2 = 0.154$; P < 0.0001) between the \log_2 fold change values of the significantly altered BEC proteins and corresponding RNAs when comparing aged (18-month-old and 19-month-old, respectively) to young (3-month-old) mice (Fig. 1e). Using 3-month-old animals as a reference, there was a steady increase in the number of significantly altered proteins from three (6 months) to 57 (12 months) to 339 proteins (18 months) (false discovery rate (FDR) P < 0.05) (Fig. 1f and Supplementary Table 2), consistent with previous bulk RNA-seq studies on whole organs and BECs that found a large number of differentially regulated genes in old compared to young mice^{45,46}. Unexpectedly, several neurofilament (Nefm, Nefl and Ina) and myelin sheet (Mog, Mbp and Plp1) proteins, although being strongly depleted in BECs compared to FT (Fig. 1f, right panel), were upregulated in the BEC proteome during aging (Fig. 1f, volcano plots). Immunolabeling and electron microscopy analysis of isolated BECs and brain capillaries confirmed the endothelial localization of Mbp and the engulfment of multi-lamellar membranous structures by aged endothelium, respectively (Fig. 1g). These results are in line with recent findings showing that microvascular endothelial cells act as 'amateur' phagocytes to engulf myelin debris⁴⁷ and contribute to the degradation of neurofilaments during aging^{48,49}.

Age-related protein expression dynamics

Genes with similar expression dynamics have been shown to share biological functions⁵⁰. To characterize the temporal profile of age-related BEC protein levels in greater detail, we first clustered all identified proteins based on their abundance patterns across timepoints (3 months. 6 months, 12 months and 18 months of age). Unsupervised clustering using Bayesian non-parametric time series modeling revealed 16 clusters that varied in size between 44 and 312 identified proteins and between six and 119 significantly altered proteins (Fig. 2a). Notably, several of the most abundant clusters showed opposing trends in their abundance dynamics during aging (Fig. 2b and Extended Data Fig. 1). To identify possible links between BEC protein dynamics and function, we categorized significantly altered proteins in each cluster according to their SL and biological processes (BPs) using Gene Ontology (GO) terms. As illustrated by clusters 1-4, there was a segregation of clusters with individual GO terms and an alignment between SLs and corresponding BPs (Fig. 2a).

Focusing on significantly enriched BPs, we found a more than five-fold enrichment of proteins related to 'translation' (for example, Rpl and Rps) in cluster 9, which was characterized by temporary downregulation at 12 months of age (Fig. 2a–c). 'RNA splicing'-related proteins (for example, Srsf) were enriched in cluster 3, showing a continuous downregulation until 18 months of age. In contrast, proteins related to 'oxidation reduction' (for example, Prdx5) and 'lipid metabolism' (for example, Fasn) were enriched in cluster 4, which exhibited significant upregulation at 18 months of age. Proteins related to 'cytoskeleton organization' (for example, Vcl and Pxn) and 'cell adhesion' (for example, Ctnnd1 and Tjp1/2) were enriched

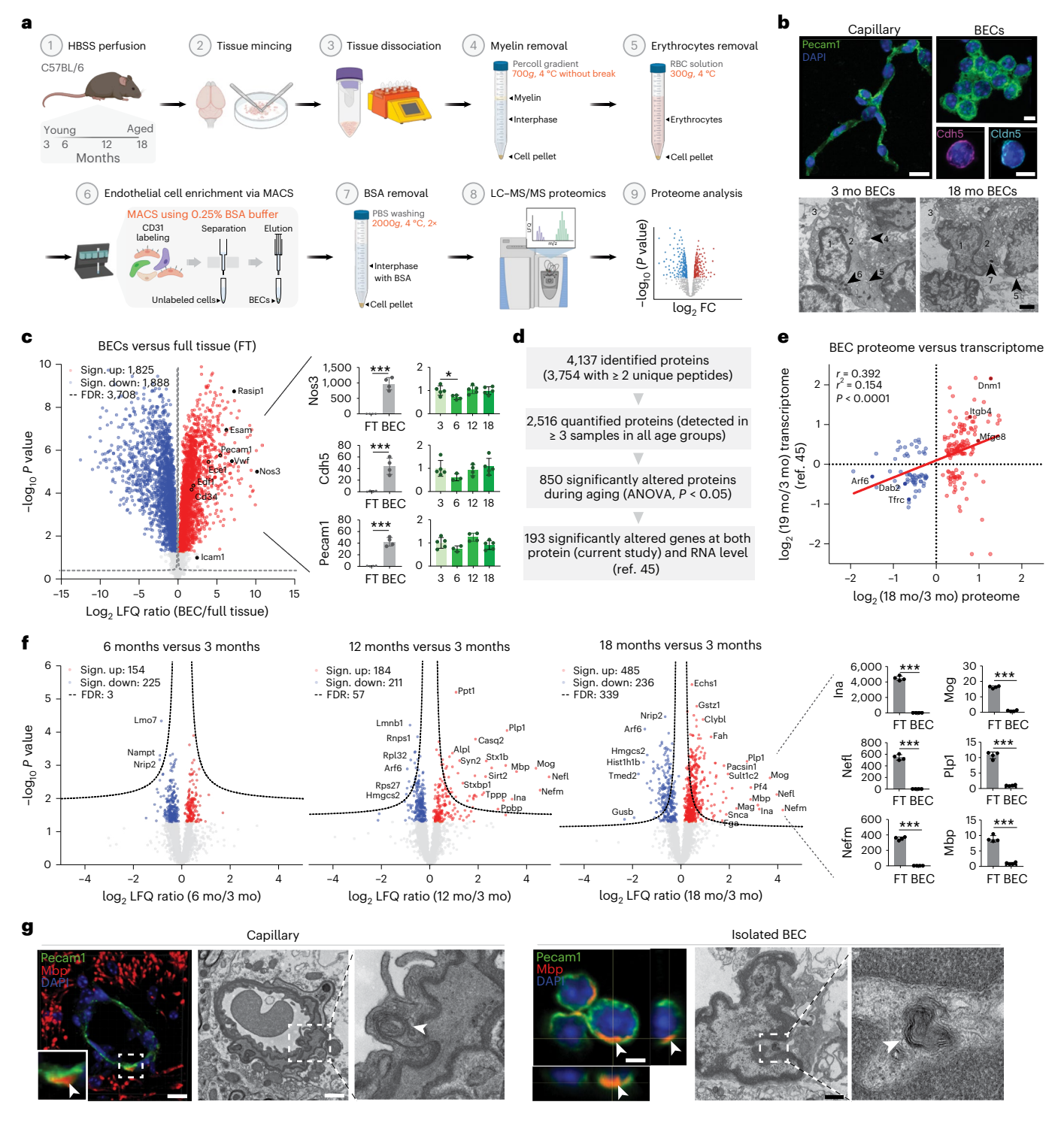


Fig. 1| Proteomic analysis of mouse BECs during aging. a, Protocol for isolation of BECs for proteomics. b, Top, isolated capillaries (scale bar, $10 \mu m$) and BECs (scale bar, $5 \mu m$) stained for CD31, Cdh5 and Cldn5. Bottom, ultrastructure of isolated BECs from 3-month-old and 18-month-old mice (scale bar, $1 \mu m$) (1 = nucleus, 2 = cytoplasm, 3 = cytoplasmic protrusions, 4 = mitochondria, 5 = vacuoles, 6 = lysosomes, 7 = membrane inclusion). c, Left, volcano plot shows enrichment of endothelial marker proteins (labeled with their gene name) in BEC preparations compared to FT (n = 4 mice per group). Right, relative abundance of Nos3, Cdh5 and Pecam1 proteins in BECs (normalized to FT) and across different timepoints (normalized to 3 months). d, Summary of the LC-MS/MS and LFQ results. e, Correlation between age-related changes of the BEC proteome (current study) and transcriptome⁴⁵, focusing on overlapping significantly altered genes in both datasets. Red line marks simple linear regression (P < 0.0001). f, Left, volcano plots show protein abundance changes during BEC aging (compared

to 3 months of age, n=4-5 mice per group). Proteins showing the highest or most significant changes in abundance are marked with their gene names. Right, relative abundance of neurofilament and myelin marker proteins in BECs (normalized to FT). ${\bf g}$, Ultrastructural images of Mbp localization and multilamellar membranous structure engulfment (white arrowheads) by aged mouse brain endothelium in brain capillary (scale bar, $1\,\mu$ m) and isolated BEC (scale bar, $1\,\mu$ m (confocal) and 200 nm (electron microscopy, EM)). ${\bf b}$, ${\bf g}$, Experiments were repeated six times. ${\bf c}$, ${\bf f}$, $-\log_{10}$ -transformed P value plotted against the \log_2 -transformed protein LFQ ratio for each protein. Comparison by two-tailed unpaired t-test. Dotted lines mark FDR threshold (P<0.05). Red and blue color indicate significant (P<0.05) enrichment and depletion, respectively. Bar graphs represent mean values \pm s.d.; data points are from individual animals (*P<0.05, ****P<0.001). The exact P values are presented in Source Data file for Fig. 1. mo, months; Sign., significant.

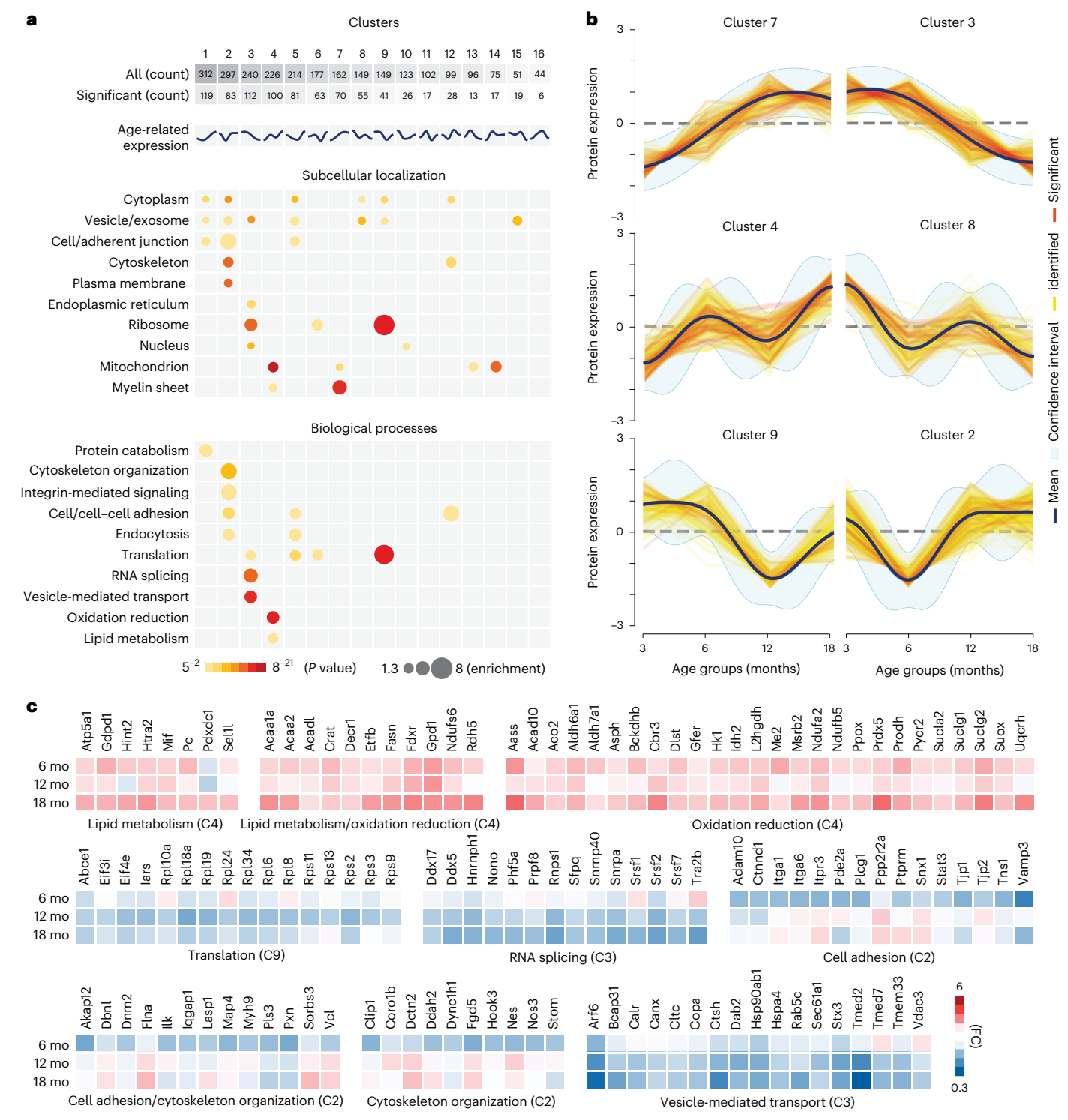


Fig. 2 | Unsupervised clustering of age-related protein dynamics of BECs. a, Enrichment analysis of SL and BPs of significantly altered proteins by clusters based on GO terms (FDR P < 0.05). Clusters were determined by the DPGP mixture model on the zero-transformed mean $\log_2 \text{LFQ}$ values. b, Exemplary clusters illustrating variations in the pattern of age-related protein abundance

changes (blue line: cluster mean; light blue band: confidence interval; yellow line: all quantified; red line: significant protein abundance in each cluster). \mathbf{c} , Heat map of significantly altered proteins according to BPs and selected clusters ordered by directionality of change (normalized on 3 months) (comparison by ANOVA followed by Tukey's multiple comparisons test, P < 0.05). C, cluster.

in cluster 2, showing temporary downregulation at 6 months of age. 'Vesicle-mediated transport' proteins (for example, Arf6 and Tmed2) were enriched in cluster 3 and showed a continuous downregulation during aging (Fig. 2a–c), whereas the 'vesicle/exosome' SL was represented in multiple clusters with vastly different profiles (Fig. 2a). Collectively, these findings demonstrate close links between

age-related protein abundance dynamics and individual BPs, including vesicle-mediated transport pathways.

BEC proteins implicated in endothelial vesicular transport

Given the central role of BECs in maintaining BBB integrity and recent data showing an age-related shift from ligand-specific

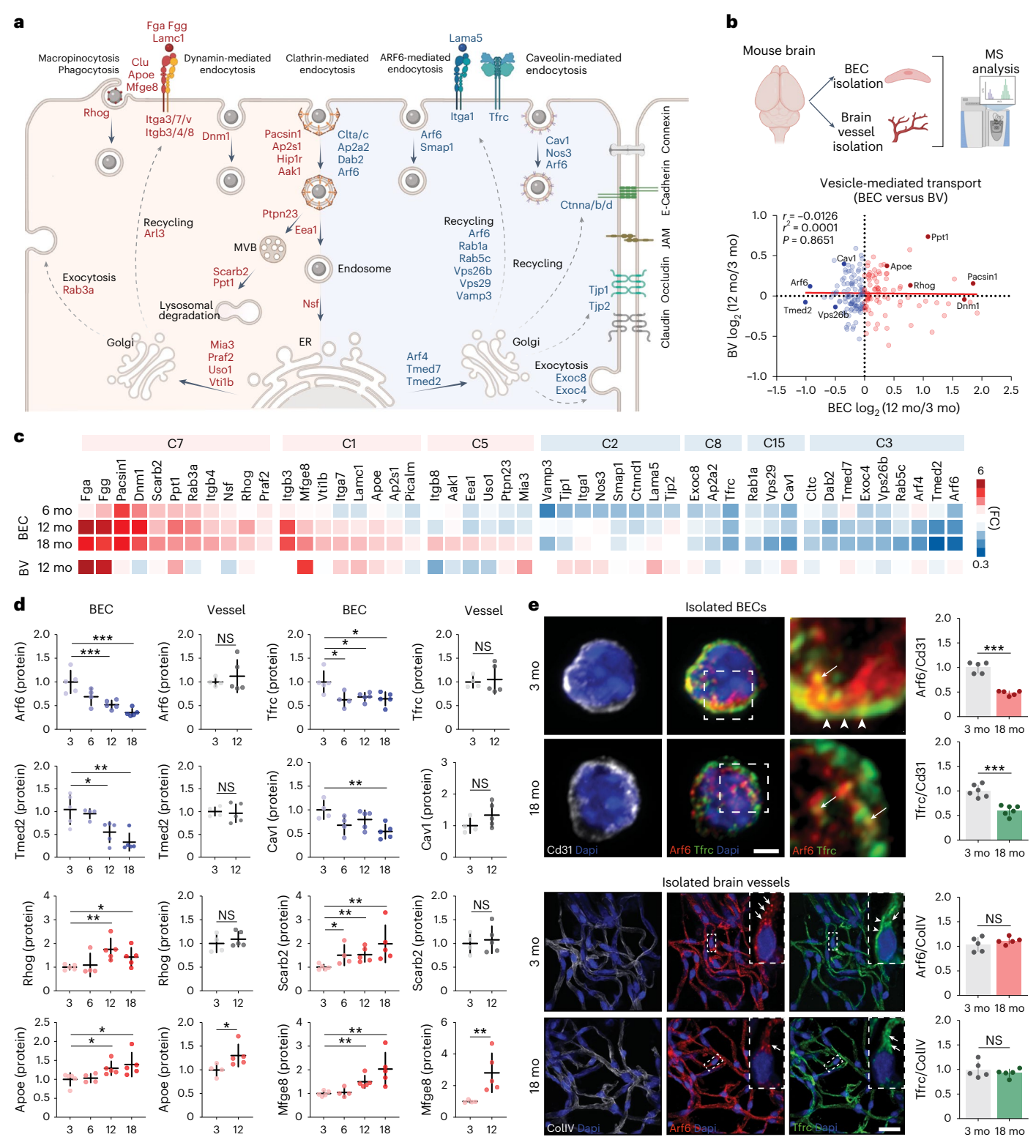


Fig. 3 | **Age-related changes of BEC proteins implicated in vesicular transport. a**, Endothelial vesicle-mediated transport pathways and associated proteins that were significantly upregulated (red) or downregulated (blue) in BECs during aging (ANOVA, P < 0.05, n = 5 mice per group). **b**, Age-related proteomic analysis and the lack of correlation between vesicle-mediated transport proteins of BECs compared to whole BV. Red line marks simple linear regression. **c**, Comparison of age-related proteome changes of endothelial vesicle-mediated transport in BECs versus BV. BECs: comparison by ANOVA followed by Tukey's multiple comparisons test (P < 0.05). Vessels: comparison by two-tailed unpaired t-test

(P < 0.05). **d**, Detailed results of selected proteins (n = 4-5 mice per group). **e**, Immunocytochemistry and quantification of Arf6 and Tfrc in isolated BECs (scale bar, $2 \mu m$) and isolated brain vessels (scale bar, $20 \mu m$) of young and aged mice (n = 5-6 mice per group). White arrows and arrowheads indicate the cytoplasmic and membrane localization of Tfrc, respectively. **d**, **e**, Comparison by two-tailed unpaired t-test (P < 0.05). Graphs represent mean values $\pm s$.d.; data points are from individual animals (*P < 0.05), *P < 0.01; ***P < 0.001; NS, not significant). The exact P values are presented in the Source Data file for Fig. 3. CollV, Collagen V; MVB, multi-vesicular body.

receptor-mediated to non-specific caveolar transcytosis³⁰, we next turned to vesicle-mediated transport proteins and transmembrane receptors (Fig. 3a and Supplementary Table 2).

Focusing on vesicle-related proteins, we found major regulators of macropinocytosis (Rhog), dynamin-mediated endocytosis (Dnm1). exocytosis (Rab3a), multi-vesicular body formation (Ptpn23) and lysosomal degradation (Scarb2 and Ctsd) to be upregulated with aging, whereas the main vesicle-coating proteins (Arf6, Clta/c and Cav1) were downregulated (Fig. 3a). Of the 20 exocytosis-related proteins, 16 proteins were positive regulators of exocytosis and showed increased protein abundance, suggesting an increased level of exocytosis during endothelial aging (Supplementary Table 2). Endothelial nitric oxide synthase (Nos3), a regulator of caveolin-mediated endocytosis⁵¹, was transiently downregulated, Endoplasmic reticulum (ER)-Golgi vesicle-mediated transport encompassed proteins that were upregulated (Mia, Uso1 and Vti1b) and downregulated (Tmed2 and Tmed7) with aging, as were regulators of clathrin-mediated endocytosis (upregulated: Pacsin1, Hip1r, Aak1 and Ap2a1; downregulated: Dab2, Ap2a and Arf6).

Focusing on endothelial receptors, we found that multiple subunits (Itga3/7/v and Itgb3/4/8) and ligands (Mfge8, Lamc1 and Fga/Fgg) of the integrin receptor complex were upregulated with aging, whereas transferrin receptor (Tfrc), the Itga1 receptor subunit and Lama5 ligand exhibited an aged-related transient downregulation (Fig. 3a). To further check whether the reduction in Tfrc levels is due to an age-related increase in receptor shedding, we performed single tryptic peptide analysis at 18 months versus 3 months of age. In total, we found two and 13 peptides from the intracellular and extracellular regions, respectively, to be significantly downregulated to a similar extent in aged BECs, arguing against altered Tfrc shedding (Extended Data Fig. 2). The tight junction scaffolding proteins Tjp1 and 2 and the adherent junction protein Ctnnd were likewise downregulated during aging.

We next explored the specificity of age-related protein changes of vesicle-mediated transport in BECs compared to the whole brain vasculature (BV) and found no correlation between the two preparations (Fig. 3b and Supplementary Table 3). Specifically, Arf6, Tfrc, Tmed2, Cav1, Rhog and Scarb2, which were among the most significantly dysregulated proteins in BECs, were not significantly altered in BV during aging. In contrast, Mfge8 (milk fat globule-EGF factor-8, also known as lactadherin) and Apoe were significantly upregulated in both BEC and brain vessel preparations (Fig. 3c,d), consistent with their role as ligands of the integrin receptor complex.

The most significantly downregulated protein in BECs was Arf6 (ANOVA, FDR q = 0.002), a key regulator of clathrin-dependent, caveolin-dependent and clathrin-independent, caveolae-independent endocytosis, as well as vesicle-mediated recycling of transmembrane receptors and junction proteins 52,53 (Fig. 3a).

 $\textbf{Fig. 4} \,|\, \textbf{Effects of endothelial Arf6 on vesicular transport and mRNA processing.}$

a, Gene deletion and overexpression experiments on Arf6 in mice. b, Volcano plot showing differences in mouse BEC protein abundance between endothelial Arf6-deficient and WT mice (n = 8 mice per group). c, Summary of the LC-MS/MS results and enrichment analysis of significant downregulated proteins. d, Heat map of the top 27 most significantly altered vesicle-mediated transport proteins in Arf6-KO mouse BECs. e, Gene deletion and overexpression experiments on Arf6 in human iECs. f, Volcano plot showing differences in protein abundance between ARF6-deficient and WT cells (n = 6 samples per group). **g**, Summary of the LC-MS/MS results and enrichment analysis of significant downregulated proteins. h, Heat map of the top 27 most significantly altered vesicle-mediated transport proteins in ARF6-KO human iECs. i, Confocal validation of endothelial recombinant protein expression in AAV-treated mouse brain (scale bar, 20 µm). Arrows indicate GFP-positive endothelial cells. j, Confocal imaging and quantification of FM1-43X endocytosis in iECs (scale bar, 20 μm; comparison by two-tailed unpaired t-test, ***P < 0.001). Arrows indicate FM1-43FX-positive vesicles. i, j, Graphs represent mean values ± s.d.; data points are from individual images. k, Volcano plot showing differences in mouse BEC protein abundance

To validate the age-related reduction of Arf6 levels, we performed immunocytochemistry on isolated BECs prepared from aged (18-month-old) and young (3-month-old) mice. Co-staining for Arf6 and Tfrc along with Pecam1 confirmed their BEC-specific reduction during aging, with some evidence for a shift in the cellular distribution of Tfrc in isolated aged BECs (Fig. 3e). In contrast, immunocytochemical analysis of isolated brain parenchymal vessels for Arf6 and Tfrc along with Collagen V showed no significant age-related alteration (Fig. 3e), which, however, agrees with the vessel proteomics data (Fig. 3d).

These findings emphasize the importance of cell-type-specific proteomics for studying vesicular transport mechanisms during aging. They further highlight the candidacy of Arf6 in mediating age-related protein changes of endothelial vesicle-mediated transport and the recycling of transmembrane receptors.

Endothelial Arf6 and vesicle-mediated transport pathways

To better understand the role of Arf6 in BECs, we conducted gene deletion and overexpression experiments. We first performed proteomic analyses in mice with endothelial cell (EC)—specific Arf6 deficiency and in human induced endothelial cells (iECs) derived from ARF6-KO induced pluripotent stem cells (iPSCs) (Fig. 4a,e, top, and Extended Data Figs. 3 and 4). We found a 30% reduction of Arf6 levels in EC-Arf6-KO BECs, whereas Arf6 was not detected in Arf6-KO iPSCs (Fig. 4b,f). In total, 312 and 1,724 proteins were significantly altered in BECs and iECs, respectively (Supplementary Tables 4 and 6). Enrichment analyses of significantly downregulated proteins showed mRNA processing and splicing to be among the most affected BPs in both models (Fig. 4c,g), consistent with our findings on the aged BEC proteome (Fig. 2). Moreover, chromatin remodeling and nucleosome assembly related proteins were likewise downregulated in mouse and human, respectively, in line with the previously published role of Arf6 in cell division 54.

Focusing on vesicle-mediated transport proteins, we found a similar proportion of proteins being upregulated and downregulated upon Arf6 deletion in mice (Fig. 4b,d) whereas, in ARF6-deficient iECs, there was an overrepresentation of upregulated proteins (120 of the 184 vesicle-mediated transport proteins) (Fig. 4f,h). We, therefore, performed functional experiments in ARF6-KO iECs and found an increased level of endocytosis (FM1-43FX in newly formed vesicles). This upregulation of endocytosis despite Arf6 deletion potentially reflected a compensatory response (Fig. 4j).

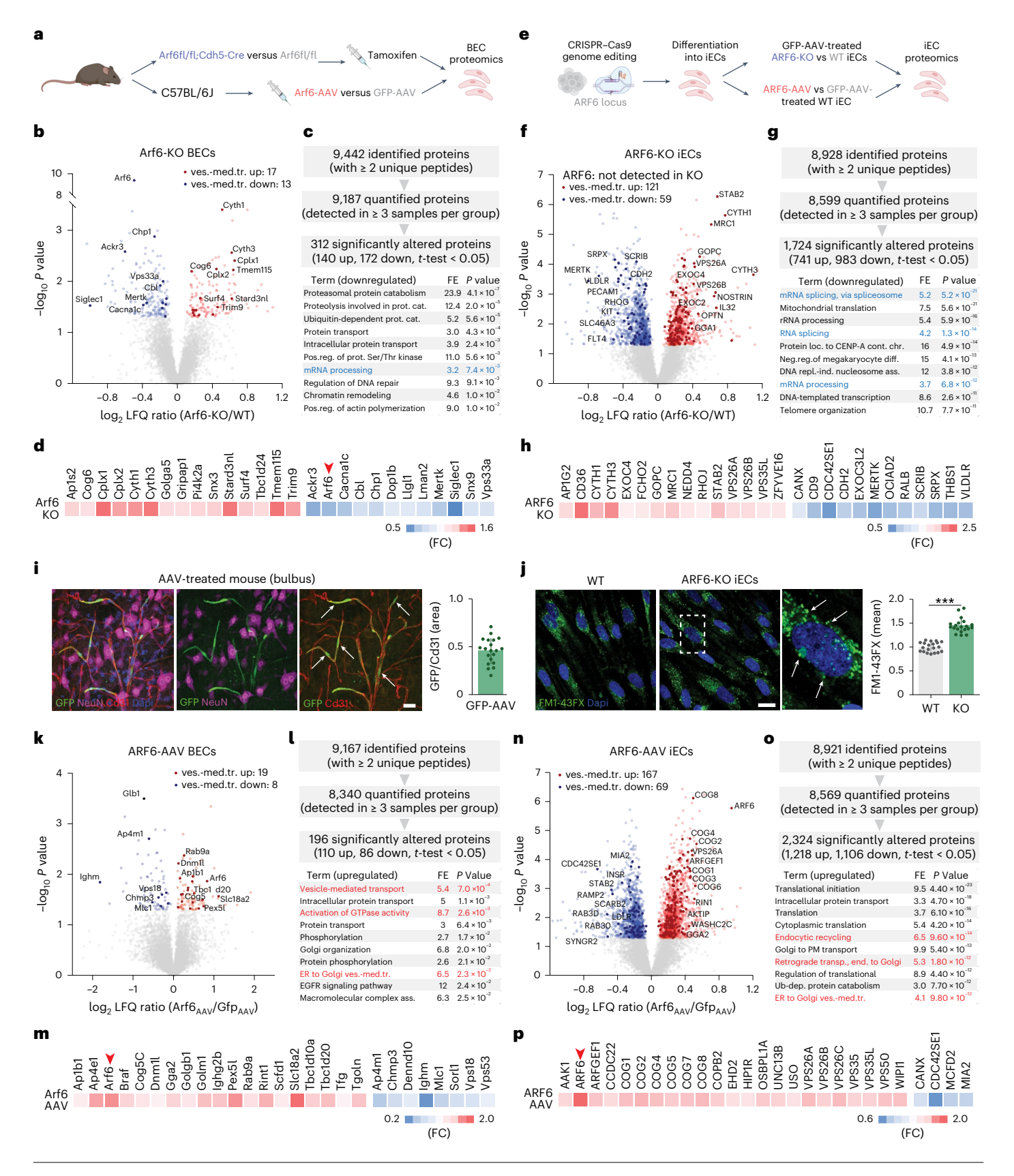
To further investigate consequences of Arf6 modulation, we performed overexpression experiments by infecting mice with BEC-specific⁵⁵ Arf6-GFP-AAV or GFP-AAV (used as control), followed by BEC proteomics (Fig. 4a, bottom, and Supplementary Table 5). To validate the specificity of the virus and the efficiency of virus transduction, we performed immunohistochemistry on the olfactory bulb region of GFP-AAV-treated mice and found that 45% of the CD31-labeled

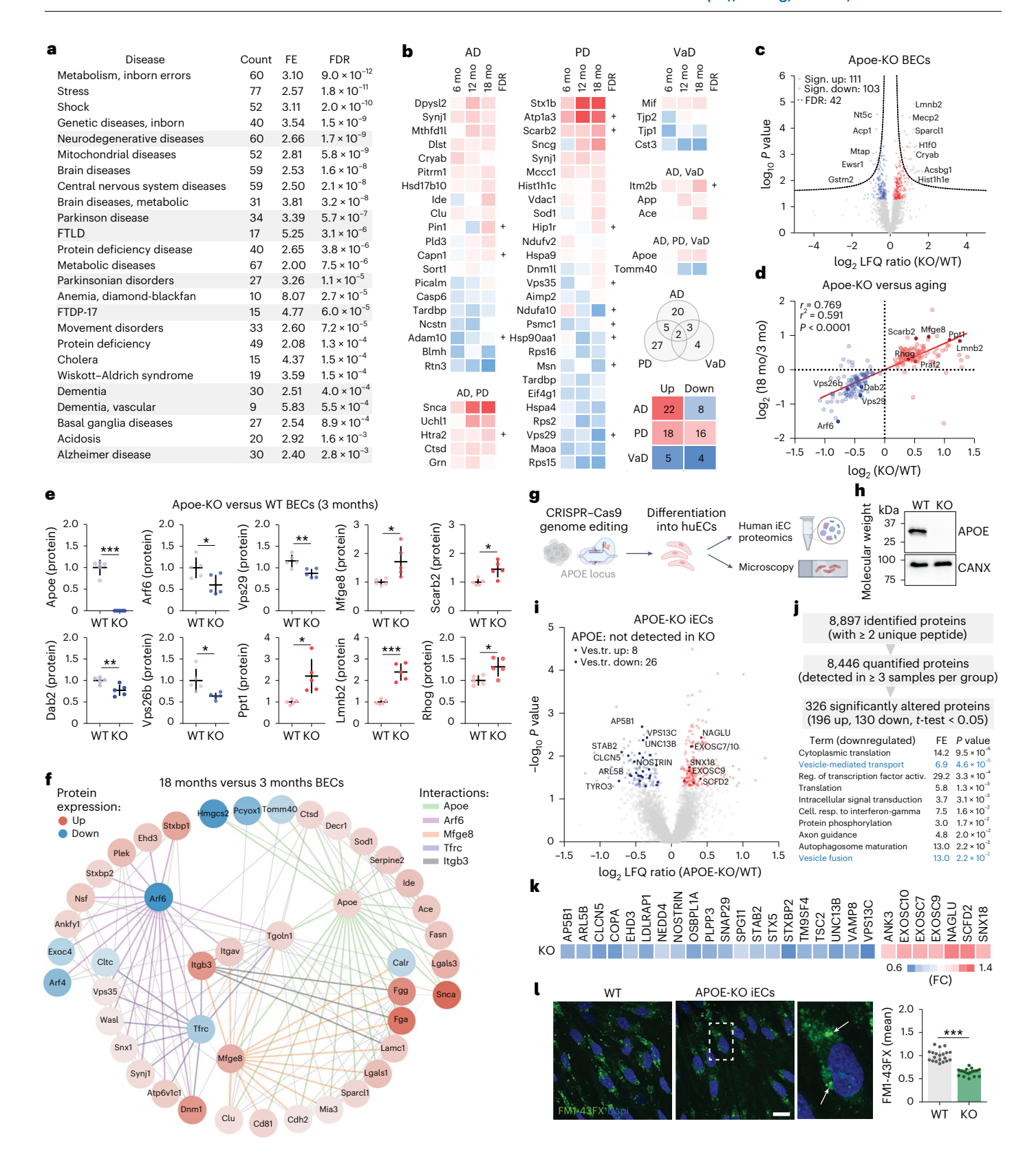
between Arf6-treated and Gfp-AAV treated mice (n = 4 samples per group). I, Summary of the LC-MS/MS and LFQ results and enrichment analysis of significantly upregulated proteins. m, Heat map of significantly altered vesiclemediated transport proteins. n, Volcano plot showing differences in protein abundance between ARF6-treated and GFP-AAV treated human iECs (n = 6samples per group). o, Summary of the LC-MS/MS results and enrichment analysis of significantly upregulated proteins. p, Heat map of the top 27 most significantly altered vesicle-mediated transport proteins. **b**, **f**, **k**, **n**, The –log₁₀transformed P value is plotted against the log₂-transformed protein LFQ ratio for each protein. Vesicle-mediated transport proteins are highlighted in darker color. **b**,**d**,**f**,**h**,**k**,**m**,**n**,**p**, Comparison by two-tailed unpaired t-test (P < 0.05). Red and blue color indicate significant enrichment and depletion, respectively. The exact Pvalues are presented in the Source Data file for Fig. 4. ass., assembly; cont. chr., containing chromatin; diff., differentiation; end., endosome; FE, fold enrichment; loc., localization; neg.reg., negative regulation; pos.reg., positive regulation; prot. cat., protein catabolism; prot. Ser/Thr kinase, protein serine/threonine kinase; repl.-ind., replication induced; transp., transport; Ub.-dep., ubiquitin-dependent; ves.-med.tr., vesicle-mediated transport.

vasculature was GFP positive (Fig. 4i). Proteomic analysis confirmed a 1.7-fold increase of Arf6 levels in BECs (Fig. 4k). Enrichment analysis of significantly upregulated proteins revealed vesicle-mediated transport, activation of GTPase activity and ER-to-Golgi vesicle-mediated transport to be among the most significantly affected BPs (Fig. 4k,m). Aside from the small GTPase Arf6, both the small GTPase-binding

protein Gga2 and the small GTPase-activating protein Tbc1d20 were upregulated. The most significantly downregulated protein was Glb1, a marker of cellular senescence and aging (Fig. 4k).

ARF6 overexpression in iECs was done with Arf6-GFP-AAV versus GFP-AAV treatment and resulted in a 1.9-fold increase of ARF6 levels (Fig. 4e, bottom, Fig. 4n,p and Supplementary Table 6). As in





Arf6-GFP-AAV-treated mice, enrichment analysis of significantly upregulated proteins revealed vesicle-mediated transport-related GO terms to be among the most prominently affected BPs (Fig. 4n,o). Specifically, ARF6 and its binding protein GGA2, DNM1L and the conserved oligomeric Golgi (COG) complex subunit COG5 were upregulated in both mouse and human (Fig. 4m,p). In fact, several subunits of COG were among the most prominently upregulated proteins in iECs (Fig. 4p).

Apoe deficiency results in a signature of accelerated BEC aging To explore potential relationships between age-related BEC proteome changes and human brain disorders, we next applied overrepresentation analysis (ORA) on disease-related databases. Focusing on BEC proteins that were altered during aging (ANOVA, P < 0.05), we found an overrepresentation (FDR P < 0.05) of disease terms related to neurodegenerative disease (eight of the top 25 disorders, highlighted

Fig. 5 | **Apoe deficiency causes a proteomic signature of accelerated BEC aging. a**, ORA of human brain diseases (count, number of significantly altered proteins; ER, enrichment ratio; neurodegenerative disorders highlighted in gray). **b**, Individual protein changes related to AD, PD and VaD during BEC aging (normalized to 3 months of age; comparison by ANOVA followed by Tukey's multiple comparisons test, P < 0.05). **c**, Volcano plot showing differences in mouse BEC proteome of 3-month-old Apoe-deficient and WT mice (n = 8 mice per group). Dotted lines mark an FDR threshold (P < 0.05, n = 5 mice per group). **d**, Correlation of \log_2 -transformed protein LFQ ratios that were significantly dysregulated in BECs from Apoe-KO and 18-month-old WT animals compared to 3-month-old WT animals. Red line marks a simple linear regression (P < 0.0001). **e**, Detailed results of selected proteins in 3-month-old Apoe-KO mice compared to WT mice. **f**, Interaction network of Arf6 and Apoe proteins with associated proteins that were significantly dysregulated in BECs at 18 months versus 3 months of age. Colored edges indicate the interaction of hub proteins.

g, CRISPR–Cas9 genome editing and differentiation of human iPSCs to iECs. h, Western blot validation of APOE-KO iPSCs (experiment was repeated four times). i, Volcano plot shows protein abundance changes between APOE-KO and WT iECs (n=5-6 samples per group). Vesicle-mediated transport proteins are highlighted with darker color. j, Summary of the LC–MS/MS results and enrichment analysis of significantly downregulated proteins. k, Heat map of the top 27 most significantly altered vesicle-mediated transport proteins. l, Confocal imaging and quantification of FM1-43X endocytosis (scale bar, 20 μ m). c,e,f,i,k,l, Comparison by two-tailed unpaired t-test (P< 0.05). b,c,f,i,k,l, Red and blue: significantly upregulated and downregulated proteins, respectively. e,l, Graphs represent mean values \pm s.d.; data points are from individual mice (e) or images (l) (*P< 0.05, **P< 0.01; ***P< 0.001). The exact P values are presented in the Source Data file for Fig. 5. activ., activation; cell. resp., cellular response; huECs, human endothelial cells; reg. regulation.

in gray in Fig. 5a). Among these terms were Alzheimer's disease (AD), Parkinson's disease (PD) and vascular dementia (VaD), which have previously been related to vascular or endothelial processes^{56–58}. Hence, we focused on these conditions. Overall, we found 30 AD-associated (23 up, seven down), 34 PD-associated (18 up, 16 down) and nine VaD-associated (five up, four down) proteins to be significantly dysregulated during aging (Fig. 5b). Although the disease-related association does not imply that these proteins are directly causative of neurodegenerative diseases, many of them are known risk genes for AD, PD or VaD (for example, App, Snca or Apoe). Apoe and Tomm40, which were upregulated and downregulated in BECs during aging, respectively, were associated with all three conditions (Fig. 5b). Given the widely recognized role of Apoe in brain cellular aging 59-62, and of Apoe deficiency in causing endothelial dysfunction⁶³⁻⁶⁵, we next compared the BEC proteomes of young (3-month-old) Apoe-KO and wild-type (WT) mice (Supplementary Table 7). Using proteomics, 111 and 103 proteins were significantly (P < 0.05) upregulated and downregulated, respectively, in Apoe-KO mice (Fig. 5c). Comparing the BEC proteomic signature of young Apoe-KO mice with the signature of aged (18-month-old) WT mice, we found a positive correlation $(r = 0.769; r^2 = 0.501, P < 0.0001)$, suggesting an accelerating effect of Apoe deficiency on BEC aging. Notably, Arf6 was significantly downregulated in young Apoe-KO mice (fold change: 0.58) (Fig. 5d). Directionally consistent changes in young Apoe-KO and aged WT mice were further seen for several other proteins implicated in endothelial vesicle-mediated transport (Fig. 5d.e).

Focusing on the Arf6–Apoe interaction network in aged mice, we found 19 and 24 significantly altered proteins at 18 months compared to 3 months of age to exhibit direct experimentally determined connections with Arf6 and Apoe, respectively (Fig. 5f; for details, see Methods). The vesicular transport protein Tgoln1 (trans-Golgi network integral membrane protein 1) showed a direct relationship with both Arf6 and Apoe. Notably, Mfge8 and Apoe showed multiple shared connections, as did Arf6 and Tfrc. In addition, the integrin (Itgav/b3) receptor ligands Mfge8, Lamc1 and Fga/Fgg all had a direct connection with Apoe and Tgoln1.

Among the AD-related proteins, we found App (amyloid-β precursor protein) to be upregulated during BEC aging at 12 months versus 3 months of age. In addition, the App processing proteins Itm2b (integral membrane protein 2B) and Htra2 (serine protease HTRA2, mitochondrial) were likewise upregulated with BEC aging (Fig. 5b).

Some of the documented effects of Apoe deficiency on endothelial cells are mediated through systemic effects in Apoe-KO mice, including hyperlipidemia ^{63,64}. To identify cell-autonomous effects of APOE in endothelial cells, we next applied genome editing in human iPSCs to obtain a human APOE-KO line and differentiated these cells into iECs (Fig. 5g,h and Extended Data Figs. 5 and 6). Proteomic analysis revealed 326 significantly altered proteins between APOE-KO and WT iECs (Fig. 5i and Supplementary Table 8). Enrichment analysis of significantly downregulated proteins showed vesicle-mediated

transport and vesicle fusion to be among the most significantly affected BPs (Fig. 5j). Specifically, among the 28 significantly altered vesicle-mediated transport proteins, 23 were downregulated (Fig. 5k). Accordingly, we found reduced levels of endocytosis of FM1-43FX in newly formed vesicles in APOE-KO iECs (Fig. 5l). Collectively, our in vivo findings highlight the relevance of age-related BEC proteome changes for human disease and a signature of accelerated BEC aging in 3-month-old Apoe-KO mice. They further suggest cell-autonomous effects of APOE in human endothelial cells. However, a more comprehensive understanding of EC-autonomous regulation by Apoe would require further experiments.

Discussion

Using a mass spectrometry–compatible protocol for BEC enrichment, we provide an unbiased characterization of the mouse BEC proteome during aging.

Unsupervised clustering revealed distinct patterns of age-related protein expression dynamics that segregated with biological functions and SLs. We provide insights into endothelial pathways of vesicular transport, highlighting key regulators (for example, Arf6), ligands and cargos. We also present evidence for an accelerating effect of Apoe deficiency on BEC aging and a cell-autonomous role of APOE in human endothelial cells. We further offer a publicly available resource and searchable database of age-related protein dynamics of mouse BECs (available at http://becaging.de) for wider use.

Among the most prominent changes was a decline in the abundancy of proteins implicated in vesicle-mediated transport. Several observations point to a possible role of Arf6, the most significantly downregulated protein in our dataset, in mediating these changes. First, Arf6, a small GTPase, is a key regulator of membrane trafficking, endocytosis and vesicle-mediated recycling of transmembrane receptors and junction proteins 52,66,67. Second, Arf6 was co-regulated with proteins implicated in clathrin-mediated endocytosis (Cltc and Dab2)⁶⁸, vesicular transport from ER to Golgi (Arf4, Tmed2 and Tmed7) and receptor recycling (Rab5c and Vps26b), all of which were continuously downregulated with aging. Third, downregulation was further seen for Cav1 lipid raft protein, which, together with Arf6, is implicated in caveolin-mediated endocytosis⁶⁶ and further regulates the expression of Tjp1 (ref. 69). Experiments in Chinese hamster ovary cells transfected with a dominant negative Arf6 mutant have shown a redistribution of Tfrc from the cell surface to vesicles and reduced receptor recycling⁶⁸. In accordance with this, we found a similar redistribution of Tfrc in isolated BECs from aged mice (Fig. 3e). However, additional experiments would be needed to consolidate this observation. Of note, although Arf6 was prominently reduced in aged BECs, it was not changed in isolated brain vessels during aging. As Arf6 is expressed by multiple cell types in the brain, and because brain vessel preparations contain pericytes, glial and synaptic endings in addition to endothelial cells, the lack of a decrease in Arf6 levels in the aged vessel preparation

might relate to the overall pattern of Arf6 expression in non-endothelial vascular cell types. Further experiments would be needed to explore the cell-specific expression pattern of Arf6 during aging.

To explore the regulatory function of Arf6 on mouse and human endothelial cells, we next performed Arf6 deficiency and overexpression experiments. In unbiased bioinformatic analyses, we found mRNA processing among the most prominently downregulated BPs upon endothelial Arf6 deficiency in both mouse and human, consistent with our aged BEC proteomics data. Proteins related to vesicle-mediated transport were mostly upregulated in ARF6-KO iECs in accordance with an increased level of endocytosis detected by FM1-42FX experiments (Figs. 3 and 4). As a limitation of our Arf6-deficient mouse model, the reduction of Arf6 levels in our BEC preparations was only 30%. This moderate reduction might be due to (1) incomplete recombination efficiency after tamoxifen induction, (2) some contamination by non-endothelial Arf6-expressing cell types during MACS-based enrichment⁴⁴ or (3) endothelial endocytic uptake of Arf6-containing extracellular vesicles produced by other cell types^{70,71}. Overexpression of Arf6 resulted in vesicle-mediated transport being among the most affected upregulated processes in both mouse and human endothelial cells.

In particular, we found proteins involved in GTPase activity to be upregulated in mouse BECs, suggesting an increased activity of Arf6 small GTPase in Arf6-AAV-treated animals. Subunits of the COG complex were upregulated in human iECs, suggesting a positive regulation in the maintenance of intra-Golgi trafficking⁷². Glb1, a marker of cellular senescence^{73,74}, was among the most prominently downregulated proteins in Arf6-AAV-treated mice, with an opposite pattern in mice with endothelial Arf6 deficiency. These data align well with the prominent downregulation of Arf6 in aged BECs, further highlighting the importance of Arf6 during aging (Figs. 3 and 4).

In contrast to Arf6-related vesicular pathways, some of the major regulators of micropinocytosis (Rhog), multi-vesicular body formation (Ptpn23) and lysosomal degradation (Scarb2) were upregulated (Fig. 3a), consistent with an activation of protein degradation during aging⁷⁵. We further found constituents of both myelin (for example, Mbp, Mog and Plp1) and axons (for example, Nefl, Nefm and Ina) to accumulate in aged BECs, consistent with the previously reported role of BECs in clearing myelin debris after spinal cord injury and experimental autoimmune encephalitis^{47,76}. Interestingly, Scarb2, a regulator of lysosomal/endosomal transport, and Ppt1, a glycoprotein involved in lysosomal degradation, were likewise upregulated during aging. However, whether this relates to the degradation of myelin debris remains unknown.

Our results complement and extend RNA-seq studies on BECs during aging. Specifically, and in accordance with recent scRNA-seq data^{30,45}, we found an age-dependent downregulation of the receptor-mediated endocytosis components Tfrc, Cltc, Clta and Dab2, although Cav1, which is implicated in receptor-independent transcytosis, was likewise downregulated during BEC aging. Tfrc is the most widely studied and validated target protein for receptor-mediated transcytosis-based delivery approaches^{77,78}. Indeed, some approaches have shown promising results in clinical trials⁷⁹. Tfrc-based strategies receive growing interest for delivering therapeutics in age-related neurodegenerative diseases, including AD⁸⁰. The observed downregulation of Tfrc in aged mice suggests that these strategies might be less effective in aged organisms.

Our proteomics approach further captured processes that were not detected at the RNA level. Specifically, we found changes in the abundance of ligands and cargo (for example, of myelin proteins) originating from other cellular sources. In principle, the increased levels of ligand and cargo proteins can be due to an increase in cargo availability, an increase in endothelial phagocytosis (as suggested by upregulated Mfge8 or Apoe opsonin proteins) or a decrease in cargo digestion. Several receptor–ligand pairs, including the Mfge8, Lamc1

and Fgg/Fga ligands and the integrin receptor subunits Itga3/7/v and Itgb3/4/8, were upregulated with aging (Fig. 2a). Integrins are hetero-dimeric transmembrane proteins composed of alpha and beta subunits occurring in multiple combinations ⁸¹. We found most of the subunits to be upregulated with aging, whereas Itga1 and its ligand Lama5 were both downregulated. Fibrinogen (represented with Fgg and Fga), a blood-born protein that is synthesized by the liver, accumulated with aging possibly through interaction with its receptor Itgavb3 (ref. 82), which was likewise upregulated. In principle, this might reflect altered fibrinogen binding, intracellular uptake or extravasation.

Among the proteins that were continuously upregulated with aging was Mfge8, which is best known for its role in phagocytosis of apoptotic cells but is also implicated in neovascularization⁸³ and vascular amyloidosis^{25,84}. In the vasculature, Mfge8 is primarily expressed by mural cells and astrocytes⁸⁵. Mfge8-mediated clearance of apoptotic cells is mediated via integrin receptors on phagocytosing cells (specifically Itgavb3 or Itgavb5)^{83,86}, and we found Mfge8 and Itgavb3 to be co-regulated in BECs during aging (cluster 1). However, whether this relates to the clearance function of BECs remains to be investigated.

Our ORA on disease-related databases revealed a significant enrichment of proteins associated with neurodegenerative diseases while also highlighting Apoe, which is known to be involved in lipid metabolism, mitochondrial function and immunoregulation⁸⁷. In the BV, Apoe is primarily expressed by microglia and astrocytes⁸⁵ and, to a lesser extent, by other cells, including BECs^{85,88}. Hence, the elevated endothelial level of Apoe protein during aging might reflect its endothelial accumulation as a ligand rather than changes in production or secretion by endothelial cells. There is a broad literature on individual Apoe genotypes and cerebrovascular dysfunction, highlighting a role of pericytes²³ and also BECs⁸⁹ in mediating the effects of APOE4 on BBB function primarily through non-cell-autonomous mechanisms. Our proteomic results in 3-month-old Apoe-KO mice revealed a profile of accelerated BEC aging with several proteins involved in vesicular transport. Protein network analysis further revealed direct connections of Apoe with the Tgoln1 trans-Golgi network protein and multiple integrin receptor ligands, including Mfge8, Lamc1 and Fgg/a. These changes might, in part, relate to non-cell-autonomous mechanisms, including effects related to hyperlipidemia^{63,64}. However, proteomic and functional measurements of APOE-KO human iECs revealed a downregulation of vesicle-mediated transport and vesicle fusion-related proteins with decreased level of endocytosis, suggesting a cell-autonomous effect of APOE on endothelial vesicular transport.

Additional changes with BEC aging in terms of BPs were an overall decline of RNA splicing (cluster 3) and translation (cluster 9). We further found an increase in oxidation reduction (cluster 4), consistent with previous literature showing enhanced oxidative stress during cerebrovascular aging^{90–92}. Unsupervised clustering revealed a co-regulation of proteins implicated in cell adhesion and cytoskeleton organization, with a prominent reduction at 6 months of age (cluster 2). Among them were multiple components of the adherens junction-forming complex (Cdh5, Ctnna1, Ctnnb1 and Ctnnd1/p120) and its connecting actin filament-binding proteins (Vcl and Pxn)93. Ctnnd1/p120 regulates the degradation of Cdh5 via clathrin-mediated endocytosis⁹⁴, which was likewise downregulated during aging. The interaction between Ctnnd1/p120 and Cdh5 is required for maintenance of endothelial barrier function⁹⁵. Whether BBB integrity is compromised during normal aging is still controversial¹⁴. However, we found the expression levels of the tight junction proteins Tjp1 and Tjp2, major regulators of vascular permeability 96,97, to be likewise downregulated.

As a limitation, we could not combine fluorescence-activated cell sorting-based isolation of BECs with LC-MS/MS-based proteomics, as this would have required pooling brain samples from multiple animals, thus losing information from individual mice (for example, protein changes that are detectable only in individual samples) and reducing statistical power⁹⁸. Second, in contrast to scRNA-seq approaches,

our technique does not allow differentiating between BEC subtypes and addressing vascular zonation-specific aspects. Third, differentiation protocols of iPSCs into endothelial cells do not fully recapitulate endothelial functions and have not been well established to differentiate organ-specific endothelial cell subtypes. Furthermore. iPSC-derived endothelial cells may not completely resemble primary endothelial cell functionality in vivo⁹⁹. Fourth, our protocol did not enable parallel investigation of the mouse BEC transcriptome from the same BEC preparations, as the BEC sample purification protocol is different for transcriptomics and proteomics. Still, we integrated data from previous scRNA-seq studies on BEC aging, offering further insights, and also compared the age-related proteome changes of BECs with BVs to explore the cell specificity of the detected vesicular transport protein changes. Fifth, the mouse BEC and human iEC proteomes (concentration detection range, 3-4 and 4-6 orders of magnitude, respectively) represent an incomplete snapshot of proteins. Future improvements in LC-MS/MS technology may enable quantification of very low abundant proteins, such as transcription factors or specific signaling molecules. As a final limitation, age-related changes in murine BECs may differ from those in humans, which, however, are difficult to assess, as the isolation protocol requires freshly dissected brain tissue.

In summary, we resolved the mouse BEC proteome during aging and identified distinct patterns of age-related expression dynamics that segregated with biological functions and the SL of proteins. We provide insights into endothelial vesicular pathways, highlighting key regulators, ligands and cargo, and present evidence for an accelerating effect of Apoe deficiency on BEC aging. Our findings further imply a cell-autonomous role of APOE in human endothelial cells. Altogether, this study provides a framework for understanding key endothelial pathways during aging and serves as a resource for analyses of BEC function.

Methods

Animals

Animal experiments were performed in accordance with the German Animal Welfare Law (§4 TschG) and approved by the Government of Upper Bavaria (Vet_02-21-139). For all of our animal experiments, we used mixed gender groups in the same ratio of male and female mice in the range of 20–30 g of body weight up to 18 months of age. Animals were kept under standard conditions in a specific pathogen-free facility at 20–24 °C and 45–65% humidity on a 12-h light/dark cycle and had access to food and water ad libitum.

Brain specimens were obtained from C57BL/6J mice at 3 months, 6 months, 12 months and 18 months of age (Charles River Laboratories), from 3-month-old C57BL/6J Apoe $^{-/-}$ mice and from 3-month-old Arf6fl/fl;Cdh5(CreERT2) mice.

To enable comparisons of age-related proteomic changes with published transcriptomic datasets, age groups were selected based on the publicly available mouse maturation rate (The Jackson Laboratory, https://www.jax.org/news-and-insights/jax-blog/2017/november/when-are-mice-considered-old) and BEC transcriptomics datasets 93–96 (Fig. 1e) as follows: (1) beginning of mature adult phase (3 months of age), (2) end of mature adult phase (6 months of age), (3) middle-aged phase (12 months of age) and (4) beginning of old phase (18 months of age).

Arf6^{fl/fl};Cdh5(CreERT2) mice were obtained by crossing B6.Cg-Arf6tm1.1Gdp/J mice (The Jackson Laboratory, 028669 (ref. 100)) with Tg(Cdh5-cre/ERT2)1Rha mice (a kind gift from Ralf H. Adams, London Research Institute¹⁰¹). Arf6 deletion was induced by three intraperitoneal (i.p.) tamoxifen injections (each 0.25 mg g⁻¹ body weight, dissolved in Miglyol 812) in 2-month-old Arf6^{fl/fl}, Cre^{+/-} mice. Arf6^{fl/fl}, Cre^{-/-} mice treated with tamoxifen served as negative control. Animals were euthanized at 3 months of age.

Mice were aged in the animal facility of the Institute for Stroke and Dementia Research and housed in isolated ventilated HEPA filtered

cages (12-h light/dark cycle with ad libitum access to food and water). Tissues were harvested in parallel and during the same time of day.

Proteomic and immunocytochemical experiments were done on n = 4-8 mice per group, except proteomic analysis of BECs from AAV-treated mice, which was performed on four independent BEC isolates derived from n = 2 C57BL6J mice per group.

Tissue harvesting

For BEC isolation, mice were deeply anesthetized using ketamine (100 mg kg $^{-1}$, i.p) and xylazine (10 mg kg $^{-1}$, i.p) and transcardially perfused with 20 ml of ice-cold 1× HBSS and dissected. After perfusion, the brain was surgically removed and kept in HBSS at 4 °C for further analysis.

For immunohistochemical analysis, anesthetized animals were perfused with $1 \times$ HBSS and transcardially fixed with 4 % paraformal-dehyde (PFA). The dissected brain samples were incubated overnight in 4 % PFA for vibratome sectioning.

For vessel isolation, anesthetized animals were perfused with $1\times$ PBS, and the dissected brains were immediately frozen on dry ice and stored at $-80\,^{\circ}\text{C}$ until use.

BEC isolation

The entire brain without the olfactory bulb was used for BEC isolation. First, the brain was transferred to a petri dish placed on ice and minced with a scalpel. BECs were isolated using a modified version of the Adult Brain Dissociation Kit (Miltenyi Biotec, 130-107-677), which allows for mechanical and enzymatic tissue dissociation. After tissue homogenization and filtration through 70-µm cell strainers (Corning, 431751), myelin was removed using a 30% Percoll gradient (GE Healthcare, 17-5445-02), followed by removal of erythrocytes using Red Blood Cell Removal Solution (Miltenyi Biotec, 130-094-183). BECs were enriched from the single-cell suspension using CD31 MicroBeads (Miltenyi Biotec, 130-097-418) and MACS using a modified MACS buffer with low BSA content (L-MACS buffer, containing 0.25% BSA (BSA Fraction V, Sigma-Aldrich, 10735096001) and 2 mM EDTA (Thermo Fisher Scientific, 15575020) in PBS with calcium and magnesium (Corning, 21-030-CV)). After CD31 enrichment, the cell suspension was washed twice with PBS to remove residual L-MACS buffer, and, subsequently, pelleted cells were used for further protein extraction.

BV isolation

Brain vessels were isolated from whole cerebrum as described previously 102,103 . Brain tissue was placed on ice, minced with a scalpel and homogenized in 15 ml of cold Minimum Essential Medium (Thermo Fisher Scientific, 11095080) using a glass tissue grinder (Wheaton). After dissociation, myelin was removed using a 15% Ficoll gradient, followed by pellet resuspension in PBS with 1% BSA (BSA Fraction V, Sigma-Aldrich, 10735096001). Vessels were transferred onto a 40- μ m cell strainer (Corning, 431750) and extensively washed with cold PBS (with 250 ml). Isolated vessels were collected by washing the inverted cell strainer with PBS and centrifugation at 3,000g for 5 min.

Protein extraction

Isolated BECs and human iECs. Protein was extracted from isolated BECs and iECs with RIPA buffer containing 150 mM NaCl (Roth, 3957.1), 1 M Tris-HCl pH 7.5 (Roth, 9090.3), 1% NP40 (Sigma-Aldrich, 74385), 0.5% deoxycholate (Roth, 3484.3) and 0.1% SDS (Serva, 20765.03) and protein inhibitor cocktail (Roche, 4693159001). Samples were incubated in RIPA buffer for 30 min on ice, followed by centrifugation at 18,000g for another 30 min at 4 °C. Supernatants were collected and kept at -80 °C for further analysis.

Isolated vessels. Isolated vessels were lysed in a buffer containing 100 mM Tris-HCL pH 7.6 (Roth, 9090.3), 4% SDS (Serva, 20765.03) and 100 mM DTT (Sigma-Aldrich, 3483-12-3) by homogenization with

a dounce tissue grinder (Wheaton) and heating for 3 min at 95 °C. After lysis, samples were sonicated (30 s, amplitude 100%, duty cycle 50%) five times with intermediate cooling using a VialTweeter sonicator (Hielscher Ultrasonics). Remaining undissolved material and cell debris were removed by centrifugation at 16,000g for 15 min at 4 °C. Supernatants were collected and kept at -80 °C for further analysis.

Full brain tissue homogenization. Full tissue was homogenized in RIPA buffer containing 150 mM NaCl (Roth, 3957.1), 1 M Tris-HCl pH 7.5 (Roth, 9090.3), 1% NP40 (Sigma-Aldrich, 74385), 0.5% deoxycholate (Roth, 3484.3), 0.1% SDS (Serva, 20765.03) and protein inhibitor cocktail (Roche, 4693159001) with a TissueLyzer and 5-mm steel beads (Qiagen). Samples were homogenized at 50 Hz for 3 min, followed by 30-min incubation on ice. After RIPA incubation, samples were centrifuged at 16,000g for 30 min, and supernatants were collected and kept at $-80\,^{\circ}\text{C}$ for further analysis.

Mass spectrometry and data analysis

Sample preparation. The whole sample of acutely isolated BECs (-5 µg) and 20 µg of FT lysates according to a BCA assay were subjected to proteolytical digestion using the single-pot solid-phase enhanced sample preparation (SP3) 104 . After 1:2 dilution with water, a benzonase digestion with 12.5 units was performed to remove remaining DNA/RNA. Proteins were reduced by addition of dithiothreitol (BIOZOL) in 50 mM ammonium bicarbonate to a final concentration of 10 mM and incubation for 30 min at 37 °C. Cysteine residues were alkylated by addition of iodoacetamide (Sigma-Aldrich) to a final concentration of 40 mM and incubation for 30 min at room temperature in the dark. Afterwards, the reaction was quenched by adding dithiothreitol.

Proteins were bound to 40 µg of a 1:1 mixture of hydrophilic and hydrophobic magnetic Sera-Mag SpeedBeads (GE Healthcare) using a final concentration of 70 % (v/v) acetonitrile for 30 min at room temperature. Beads were washed four times with 200 µl of 80% (v/v) ethanol. For proteolytic digestion, LysC (Promega) was added in 20 µl of 50 mM ammonium bicarbonate with a protease to protein ratio of 1:80. Samples were incubated on a ThermoMixer (Eppendorf) for 30 min at 1,000 r.p.m. and 37 °C. Afterwards, trypsin (Promega) was added in 20 µl of 50 mM ammonium bicarbonate with a protease-to-protein ratio of 1:80, followed by an incubation for 16 h at room temperature. Beads were retained with a magnetic rack, and the supernatants were collected. Next. 20 ul of 0.1% formic acid was added to the magnetic beads, followed by sonication for 30 s in a sonication bath (Hielscher Ultrasonics). The supernatants of each sample were combined, filtered with 0.22-µm spin filters (Costar Spin-X, Corning) to remove remaining beads and dried by vacuum centrifugation. Dried peptides were dissolved in 20 μl of 0.1% formic acid. The peptide concentration after proteolytic digestion was estimated using a Qubit protein assay (Thermo Fisher Scientific).

Isolated brain vessels were processed in the same fashion with the following alterations. Subsequent to the benzonase digest, samples were immediately bound to 20 μg of the Sera-Beads mixture and alkylated, and the reaction was quenched as described. After an additional bead binding step, using a final concentration of 70% (v/v) acetonitrile, samples were further processed according to the standard SP3 protocol.

Mass spectrometry. The isolated BEC, isolated vessel and FT samples were analyzed on a nanoLC system (EASY-nLC 1200, Thermo Fisher Scientific), which was coupled online via a nanospray flex ion source (Proxeon, part of Thermo Fisher Scientific) equipped with a PRSO-V2 column oven (Sonation) to a Q-Exactive HF mass spectrometer (Thermo Fisher Scientific).

A peptide amount of 1 μ g per sample was separated on the nanoLC system using an in-house packed C18 column (30 cm × 75 μ m ID, ReproSil-Pur 120 C18-AQ, 1.9 μ m, Dr. Maisch) with a binary gradient

of water (A) and acetonitrile (B) containing 0.1% formic acid at 50 °C column temperature and a flow rate of 250 nl min $^{-1}$ (gradient: 0 min, 2% B; 3:30 min, 5% B; 137:30 min, 25% B; 168:30 min, 35% B; 182:30 min, 60% B). Full mass spectrometry spectra were acquired at a resolution of 120,000. The top 15 peptide ions were chosen for higher-energy C-trap dissociation with a normalized collision energy of 26%. Fragment ion spectra were acquired at a resolution of 15,000. A dynamic exclusion of 120 s was used for peptide fragmentation.

The comparison of acutely isolated endothelial cells and brain homogenates, Arf6-Ko mouse BECs and iPSC-derived human endothelial cells was analyzed on a nanoElute nanoHPLC, which was coupled to a TimsTOF Pro mass spectrometer with a CaptiveSpray ion source (Bruker).

An amount of 350 ng of peptides was separated on an in-house packed C18 analytical column (15 cm \times 75 μm ID, ReproSil-Pur 120 C18-AQ, 1.9 μm , Dr. Maisch) using a binary gradient of water (A) and acetonitrile (B) containing 0.1% formic acid at flow rate of 250 nl min $^{-1}$ (0 min, 2% B; 2 min, 5% B; 70 min, 24% B; 85 min, 35% B; 90 min, 60% B) and a column temperature of 50 °C. For the comparison of BEC versus FT, a standard Data-Dependent Acquisition Parallel Accumulation–Serial Fragmentation (DDA-PASEF) method with a cycle time of 1.1 s was used for spectrum acquisition. In brief, ion accumulation and separation using trapped ion mobility spectrometry (TIMS) was set to a ramp time of 100 ms. One scan cycle included one TIMS full MS scan and 10 PASEF peptide fragmentation scans. The m/z scan range was set to 100–1,700 for both MS and MS/MS scans. The ion mobility scan range was set to 1/k0 0.75–1.40.

For Arf6-KO mouse BECs and human iECs, a DIA-PASEF method was used for spectrum acquisition. Ion accumulation and separation using TIMS was set to a ramp time of 100 ms. One scan cycle included one TIMS full MS scan and with 26 windows with a width of 27 m/z covering an m/z range of 350–1,002 m/z. Two windows were recorded per PASEF scan. This resulted in a cycle time of 1.4 s.

Data analysis. The DDA raw data were analyzed by MaxQuant software (https://www.maxquant.org/, Max Planck Institute Munich) version 1.6.3.4 or version 2.0.1.0 (refs. 105,106). The mass spectrometry data were searched against a one-protein-per-gene canonical FASTA database of Mus musculus (downloads: 9 September 2020, 21,997 entries, or 10 February 2021, 21,998 entries) from UniProt. Trypsin was defined as protease. Two missed cleavages were allowed for the database search. The option first search was used to recalibrate the peptide masses within a window of 20 ppm. For the main search, peptide mass tolerances were set to 4.5 ppm and 10 ppm for the Orbitrap and TOF mass spectrometer, respectively. Peptide fragment mass tolerances were set to 20 ppm and 40 ppm for the Orbitrap and TOF mass spectrometer, respectively. Carbamidomethylation of cysteine was defined as static modification. Acetylation of the protein N-term as well as oxidation of methionine were set as variable modifications. The FDR for both peptides and proteins was adjusted to less than 1%. LFQ of proteins required at least two ratio counts of unique peptides. The option 'match between runs' was enabled with a matching time of 1 min and an ion mobility window of 0.05 1/k0.

The DIA-PASEF raw data were analyzed with DIA-NN version 1.8 software (https://github.com/vdemichev/DiaNN)¹⁰⁷ using a library-free search against a one-protein-per-gene database from either *Mus musculus* or *Homo sapiens* according to the sample type (murine database: download date 17 January 2023, 21,976 entries; human database: download date 1 March 2023, 20,603 entries). Trypsin was defined as protease, and two missed cleavages were allowed. Oxidation of methionines and acetylation of protein N-termini were defined as variable modifications, whereas carbamidomethylation of cysteines was defined as fixed modification. The precursor and fragment ion *m/z* ranges were limited from 350 to 1,001 and 200 to 1,700, respectively. Precursor charge states of 2–4 were considered. The optimal

mass accuracy for peptides and peptide fragments as well as the ion mobility tolerances were automatically determined by DIA-NN. An FDR threshold of 1% was applied for peptide and protein identifications.

The protein LFQ intensities were \log_2 transformed, and two-sided Student's *t*-tests were applied between the groups for statistical evaluation of differential protein abundance. If more than two groups were compared with each other, a one-way ANOVA test was additionally applied. To account for multiple hypotheses, a permutation-based FDR correction was applied separately for each comparison ¹⁰⁸. Only proteins with at least three valid values per group were considered for relative quantification.

Cluster analysis of protein expression changes

Time series clustering was performed using an unsupervised, non-parametric model-based method, the Dirichlet process Gaussian process (DPGP) mixture model (https://github.com/PrincetonUniversity/DP_GP_cluster)³⁹, on the zero-transformed mean log₂ LFQ values of all 2,516 quantified proteins. In brief, two important considerations in this problem are as follows: (1) selecting the 'correct' or 'optimal' number of clusters and (2) modeling the trajectory and time dependency of protein expression. A Dirichlet process can determine the number of clusters in a non-parametric manner, whereas a Gaussian process can model the trajectory and time dependency of protein expression in a non-parametric manner. Optimal clustering was selected using the 'maximum a posteriori' (MAP) criterion.

Enrichment analysis

GO enrichment analyses of SL (GOTERM_CC-DIRECT) and BPs (GOTERM_BP_DIRECT) in BEC protein expression clusters was performed with Database for Annotation, Visualization and Integrated Discovery (DAVID) version 6.8 software using all identified BEC proteins as a background dataset¹⁰⁹. We analyzed each expression cluster (1–16) separately, focusing on significantly altered proteins during aging (ANOVA, P < 0.05). Among the annotation results, we selected the significantly enriched GO terms (Fisher's exact test, FDR P < 0.05).

Enrichment analysis of human disorders in the aged BEC proteome (18 months versus 3 months of age) was performed with WebGestalt (WEB-based GEne SeT AnaLysis Toolkit) software 110 using the over-representation analysis (ORA) module with the Disease GLAD4U functional database and protein-coding genome reference dataset 111 . Among the annotation results, we selected the top 25 disease terms showing association (Fisher's exact test, FDR P < 0.05) with our input dataset.

Protein network analysis and visualization

Protein–protein interaction networks were constructed and visualized with STRING (version 11.0) and Cytoscape (version 3.8.2) software, respectively. We selected experimentally determined protein interactions having minimum medium confidence (interaction score > 0.4) in the *Mus musculus* database. The color gradients and size of nodes were set based on the fold change and P value of protein changes at 18 months compared to 3 months of age. Proteins were filtered based on the significance level of protein changes at 18 months compared to 3 months of age (t-test, P< 0.05). Additional filter settings were applied in Cytoscape (version 3.8.2) based on the gene of interest (Results).

iPSC culture

iPSC experiments were performed in accordance with all relevant local guidelines and regulations. Work was done with the female iPSC line, A18944, that is commercially available (Thermo Fisher Scientific, A18945). iPSCs were maintained on vitronectin-coated (Thermo Fisher Scientific, A14700) culture plates and grown until reaching 80% confluency in Essential 8 Flex Medium (Thermo Fisher Scientific, A2858501) at 37 °C with 5% CO $_2$. Cells were routinely passaged using PBS-500 nM EDTA (Thermo Fisher Scientific, 15575020).

CRISPR-Cas9 genome. A previously described single guide RNA (sgRNA) for targeting APOE exon 2 (ref. 112) was used for the genome editing. The sgRNA sequence (GGTTCTGTGGGCTGCGTTGC) was cloned into the MLM3636 plasmid (a gift from K. Joung, Addgene 43860) using the BsmBI restriction site. Genome editing was conducted as previously described¹¹³ using Cas9 plasmid pSpCas9(BB)-2A-Puro (PX459) V2.0 (a gift from F. Zhang, Addgene 62988). For electroporation, cells were dissociated using Accutase (Thermo Fisher Scientific, A1110501), transferred to Geltrex-coated (Thermo Fisher Scientific, A1413302) culture plates and grown in StemFlex (Thermo Fisher Scientific, A3349401) containing 10 mM ROCK inhibitor (Selleck Chemicals, S1049) for 2 d at a density of 150,000 cells per cm². iPSCs were transfected by electroporation as previously described¹¹⁴ with some modifications. In brief, 2 million cells were resuspended in 100 ul of electroporation solution (VWR, MIR50117) containing 20 µg of Cas9 and 5 µg of sgRNA plasmid. Cells were electroporated with two pulses at 65 mV for 20 ms in a 1-mm cuvette (Thermo Fisher Scientific, 15437270) and plated onto Geltrex-coated 10-cm plates with StemFlex medium containing 10 mM ROCK inhibitor. One day after electroporation, cells expressing Cas9 were selected with 350 ng ml⁻¹ puromycin dihydrochloride (VWR, J593) for three consecutive days, as shown previously¹¹⁵. Single-cell clone colonies were picked and analyzed by restriction fragment length polymorphism (RFLP) using NEB enzyme BbvI and Sanger sequencing, as previously described¹¹⁴.

To accommodate for improvements in the genome editing field, the previous protocol was modified for RNP-based DNA cleavage¹¹⁶ of the ARF6 locus. An sgRNA targeting ARF6 exon 2 (GGAAATGCGGATC CTCATGT) was ordered from Synthego. Similarly, for electroporation, iPSCs were seeded onto Geltrex-coated plates at a density of 150.000 cells per cm² for 2 d in StemFlex and ROCK inhibitor. To prepare the RNP complex, 60 pmol of sgRNA was mixed with 30 pmol of high-fidelity Cas9 mutant (IDT, 1081060) and incubated for 15 min at room temperature. For the electroporation, 200,000 cells were ressuspended in 20 µl of P3 Primary Cell Nucleofector Solution (Lonza, V4XP-3032) and mixed gently with the RNP complex. Cells were transferred onto one well of a nucleocuvette strip (Lonza, V4XP-3032) and electroporated in a 4D-Nucleofactor X Unit (Lonza, AAF-1002X) using the program CA137. After electroporation, cells were plated in one 12-well Geltrex-coated culture plate with StemFlex and 1× RevitaCell (Thermo Fisher Scientific, A2644501) for 2-4 d. Cells were then seeded at low density, and single-cell clone colonies were picked and analyzed by RFLP using NEB enzyme Fat I followed by Sanger sequencing, as previously described 114.

The knockouts were confirmed on protein level using either western blot analysis of RIPA lysates or proteomics, respectively. For quality control, we checked for off-target effects by polymerase chain reaction (PCR) amplification and Sanger sequencing of the top five most likely loci based on MIT and CFD scores from CRISPOR (http://crispor.tefor.net/ (ref. 117)). We also excluded on-target effects, such as loss of heterozygosity, using nearby single-nucleotide polymorphism (SNP) sequencing¹¹⁸. Lastly, pluripotency was confirmed through immunofluorescence staining of OCT4, NANOG, SSEA4 and TRA160, and chromosomal integrity was validated by molecular karyotyping (LIFE & BRAIN).

iPSC differentiation into human endothelial cells (iECs). iPSCs were seeded onto Geltrex-coated (Thermo Fisher Scientific, A1413302) cell culture plates at a density of 200,000 cells per cm² in StemFlex medium (Thermo Fisher Scientific, A3349401) containing 10 mM ROCK inhibitor (Selleck Chemicals, S1049). Differentiation was started 24 h after seeding by switching medium to Mesoderm Induction Media (STEMCELL Technologies, 05220). Medium was replenished every 24 h for 2 d. On day 3, medium was switched to APEL2 medium (STEMCELL Technologies, 05270) supplemented with 200 ng ml $^{-1}$ VEGF (PeproTech, 100-20) and 2 μ M forskolin (PeproTech, 6652995). Medium was also replenished every 24 h for 2 d. On day 5, endothelial cells were selected for CDH5 via

magnetic sorting: cells were dissociated using Accutase (Thermo Fisher Scientific, A1110501) and incubated with CDH5 MicroBeads (Miltenyi Biotec, 130-097-867) following the manufacturer's instructions. CD144 fraction was plated onto Collagen IV-coated (Sigma-Aldrich, C5533-SMG) culture plates at a density of 200,000 cells per cm² and grown in endothelial cell medium (ECM) (PromoCell, C-22011). Endothelial cells were grown until reaching 80–95% confluency and passaged with Trypsin-EDTA (Thermo Fisher Scientific, 25200056) to a ratio of 1:2–1:6. Cells were cultured up to five passages.

FM1-43FX treatment in vitro. iECs were seeded onto Collagen V-coated plates and grown until they reached confluence. Cells were incubated for 15 min at 37 °C with 5 μ g ml⁻¹ FM1-43FX (Thermo Fisher Scientific, F35355) diluted in ddH₂O. After PBS washing, cells were fixed with 4% PFA for further analysis.

AAV-based overexpression of Arf6

pArf6-EGFP (no. 49649)¹¹⁹ was obtained from Addgene. pAAV-CAG-GFP was a gift from Edward Boyden (Addgene plasmid no. 37825). pArf6-EGFP served as template to clone pArf6-2a-EGFP vectors via standard cloning techniques.

Arf6 overexpression in mouse BECs. For in vivo work, AAV particles were produced according to a previously described protocol¹²⁰. In brief, HEK293T (American Type Culture Collection, CRL-3216) cells were grown in DMEM (high glucose, GlutaMAX) supplemented with 10% FBS and 5% penicillin-streptomycin. Cells were transfected using polyethylenimine (PEI) solution with a 1:4:2 molar ratio of helper (pXX6)121, capsid (pXX2-187-NRGTEWD)55 and desired construct plasmids (pArf6-2a-EGFP or pAAV-CAG-GFP) in DPBS medium without glutamine and serum. Twenty-four hours after transfection, media was changed back to serum-supplemented DMEM, and the cells were kept for 3 d before harvesting. Supernatant was harvested at 72 h and 120 h after transfection and kept at 4 °C. Then, 120 h after cells were scraped, they were mixed with SAN + SAN digestion buffer and incubated at 37 °C in a water bath for 1 h. The supernatant was then combined with PEG solution overnight and subsequently centrifuged at 4,000g for 30 min at 4 °C. The resulting PEG pellet and cell lysate were mixed together and loaded on top of an iodoxanol gradient and centrifuged at 350,000g for 2 h and 25 min at 18 °C with slow acceleration. Once the virus was collected from the iodoxanol gradient, it was passed through an Amicon filter and washed multiple times to remove jodoxanol. After the final wash, the virus was resuspended and collected from the filter. Titers were determined using qPCR. Viral aliquots were stored at -80 °C until used. AAVs (GFP or ARF6-GFP) were administered intravenously in 2-month-old C57BL6J mice at a dose of 2×10^{10} viral particles per mouse. BECs were isolated 4 weeks after infection.

Arf6 overexpression in human iECs. For invitro work, AAV particles were produced in HEK293T cells. Cells were grown in DMEM supplemented with 10% FBS and penicillin–streptomycin until reaching 80% confluency. Upon confluency, cells were triple transfected with pHelper, pAAV-DJ (Cell Biolabs, VPK-400-DJ) and pAAV-GFP or pAAV-ARF6-GFP using PEI (pH7.0).

Cells were detached using 0.5 M EDTA in PBS, pH 7.4, 2–3 d after transfection. AAV particles were extracted using an AAVpro Purification Kit (all serotypes) (Takara, 6666), and titration was performed by qPCR using an AAVpro Titration Kit (for real-time PCR) version 2 (Takara, 6233), in both cases following the manufacturer's instructions.

Cells were seeded onto Collagen IV-coated plates at approximately 50% confluency 1 d before the AAV treatment. Twenty-four hours after seeding, cells were treated with 3×10^7 viral particles per well (GFP or ARF6-GFP) in ECM and incubated for another 48 h, when media was exchanged to ECM. Cells were collected for mass spectrometry analysis 4 d after viral infection.

Immunohistochemistry

Supplementary Table 9 specifies the primary and secondary antibodies used in the present study, including working dilutions.

Brain slices. Brain samples were embedded in 3% agarose for 100- μm coronal vibratome sectioning. Coronal free-floating sections were permeabilized and blocked using 3% BSA/Triton X-100 for 1 h at room temperature. Primary antibodies were diluted in 3% BSA in PBS and incubated overnight at 4 °C. Secondary antibodies were diluted in PBS and incubated at room temperature for 2 h. After washing, DNA was stained using DAPI (Invitrogen, D1306, 1:2,000) for 5 min at room temperature. Brain slices were mounted using Fluoromount medium (Sigma-Aldrich, F4680-25ML).

Isolated BECs. Isolated BECs were fixed in suspension using 4% PFA for 20 min at room temperature. After PFA washing via centrifugation at 2,000g for 10 min, cells were resuspended in dH_2O water, transferred onto a microscope slide (Thermo Fisher Scientific, J1800AMNZ) and dried at room temperature. Cells were blocked using 3% BSA in PBS for 1 hat room temperature. Primary antibodies were diluted in the same blocking buffer and incubated overnight at $4\,^{\circ}\text{C}$, whereas secondary antibodies were diluted in PBS and incubated for 1 hat room temperature. After washing, DNA was stained using DAPI (Invitrogen, D1306, 1:2,000) for 5 min at room temperature. BECs were mounted using Fluoromount medium (Sigma-Aldrich, F4680-25ML).

Isolated vessels. Isolated vessels were transferred onto a microscope slide (Thermo Fisher Scientific, J1800AMNZ) and dried at room temperature. Fixation and permeabilization were performed using ice-cold 100% acetone for 10 min at -20 °C, followed by blocking with 3% BSA in PBS for 1 h at room temperature. Primary antibodies were diluted in the same blocking buffer and incubated overnight at 4 °C, whereas secondary antibodies were diluted in PBS and incubated for 1 h at room temperature. After washing, DNA was stained using DAPI (Invitrogen, D1306, 1:2,000) for 5 min at room temperature. Isolated vessels were mounted using Fluoromount medium (Sigma-Aldrich, F4680-25ML).

Differentiated human endothelial cells (iECs). Differentiated endothelial cells were seeded into Collagen IV-coated (Sigma-Aldrich, C5533-5MG) coverslips and fixed with 4% PFA for 15 min at room temperature when they reached a confluent monolayer. After washing, cells were blocked using 3% BSA buffer in PBS for 1 h at room temperature. Primary antibodies were diluted in the same blocking buffer and incubated overnight at 4 °C. Secondary antibodies were diluted in PBS and incubated for 1 h at room temperature. After washing, DNA was stained using DAPI (Invitrogen, D1306, 1:2,000) for 5 min at room temperature. Coverslips with endothelial cells were mounted using Fluoromount medium (Sigma-Aldrich, F4680-25ML).

Confocal microscopy and image analysis. Fluorescent images were acquired with a Zeiss confocal microscope (LSM800, ×40 objective with Airyscan detector). Integrated density values (the product of mean gray value and area) of Arf6 and Tfrc were determined using ImageJ software (version 1.52p) (10 images per sample) and normalized to Pecam1, Col4 or Cdh5 endothelial markers according to the experiments. Statistical significance was assessed by two-tailed Student's *t*-test.

Transmission electron microscopy

Brain tissue. Mice were perfused in fixative (4% PFA and 2.5% glutaral-dehyde in 0.1 M sodium cacodylate buffer, pH 7.4; Science Services), and brains were immersion fixed for 24 h, vibratome-sectioned coronally and incubated for another 24 h in the same fixative and stored in PBS. The sections were stored in PBS at 4 °C until the start of the post-embedding. We applied a standard rOTO en bloc staining protocol¹²², including post-fixation in 2% osmium tetroxide (EMS) and 1.5%

potassium ferricyanide (Sigma-Aldrich) in 0.1 M sodium cacodylate (Science Services) buffer (pH 7.4). Staining was enhanced by reaction with 1% thiocarbohydrazide (Sigma-Aldrich) for 45 min at 40 °C. The tissue was washed in water and incubated in 2% aqueous osmium tetroxide, washed and further contrasted by overnight incubation in 1% aqueous uranyl acetate at 4 °C and 2 h at 50 °C. Samples were dehydrated in an ascending ethanol series and infiltrated with LX112 (LADD).

Isolated BECs. The isolated BEC pellet was conserved throughout all fixation, contrasting and infiltration steps. Cells were fixed for 15 min in 2.5% glutaraldehyde (EM-grade, Science Services) in 0.1 M sodium cacodylate buffer (pH 7.4) (Sigma-Aldrich) and washed three times in 0.1 M sodium cacodylate buffer before post-fixation in reduced osmium (1% osmium tetroxide (Science Services) and 0.8% potassium ferrocyanide (Sigma-Aldrich) in 0.1 M sodium cacodylate buffer). After contrasting in 0.5% uranylacetate in water (Science Services), the pellet was dehydrated in an ascending ethanol series, infiltrated in epon (Serva) and cured for 48 h at 60 °C.

Electron microscopy and image analysis. Ultra-thin sections of brain tissues and BEC pellets were generated on a Leica UC7 and deposited onto formvar-coated copper grids (Science Services) without post-contrasting. Transmission electron microscopy images were acquired on a JEM-1400Plus (JEOL) using EMplified software (TVIPS, version 0.6.10).

Western blot and quantification

Protein lysates were analyzed by SDS-PAGE and transferred to 0.2- μ m nitrocellulose membranes using a Mini-Protean and Trans-Blot system. After transfer, membranes were incubated in I-Block (Invitrogen, T2015) for 1 h at room temperature. Primary antibodies were incubated in the same buffer at 4 °C overnight and HRP-conjugated secondary antibodies for 1 h at room temperature. Detection was performed by chemiluminescence development (Immobilon ECL detection reagent, Merck Millipore) using Fusion FX7 (Vilber Lourmat). Protein levels were quantified using ImageJ Gel Analyzer (version 1.52p). Statistical significance was analyzed by two-tailed Student's t-test. The dilution of primary and secondary antibodies for western blotting is specified in Supplementary Table 9.

Statistics and reproducibility

Data collection and analysis were not randomized. Blinding was applied to immunohistochemical image analysis. For all other experiments, blinding was not possible in order to preserve the homogeneity of the measurements (tissue processing and sample analysis were conducted alternately from the samples of the different experimental groups, avoiding batch effect and reducing technical variance). All data values of the descriptive statistics are given as mean \pm s.d. unless stated otherwise. Data were analyzed using two-tailed unpaired t-test or ANOVA followed by Tukey's multiple comparisons test (indicated in each experiment, n = 4-8 samples per group). For qualitative analysis, experiments were repeated a minimum of four times (Figs. 1b,g and 5h and Extended Data Figs. 3b and 5b). No statistical methods were used to pre-determine sample sizes, but our sample sizes are similar to those reported in previous publications 102,103. Data distribution was assumed to be normal, but this was not formally tested. In addition to the previously introduced software, Microsoft Excel (2016) and Graph-Pad Prism (8.3.1) were used for additional data analysis, statistics and figure representation. In the case of APOE-KO versus WT human iEC proteomics experiment, n = 1 KO sample was excluded due to incomplete APOE deficiency.

Reporting summary

Further information on research design is available in the Nature Portfolio Reporting Summary linked to this article.

Data availability

The datasets generated through this work are available in a publicly accessible repository. The mass spectrometry proteomics data have been deposited to the ProteomeXchange Consortium via the PRIDE¹²³ partner repository with the dataset identifiers PXD045026, PXD045006, PXD045004, PXD044996 and PXD044993. All data supporting the findings described in this article are available in the article itself and in the supplementary materials and from the corresponding author upon reasonable request. Source data are provided with this article.

References

- Sweeney, M. D., Zhao, Z., Montagne, A., Nelson, A. R. & Zlokovic, B. V. Blood-brain barrier: from physiology to disease and back. *Physiol. Rev.* 99, 21–78 (2019).
- Siegenthaler, J. A., Sohet, F. & Daneman, R. 'Sealing off the CNS': cellular and molecular regulation of blood-brain barriergenesis. *Curr. Opin. Neurobiol.* 23, 1057–1064 (2013).
- 3. Iadecola, C. The neurovascular unit coming of age: a journey through neurovascular coupling in health and disease. *Neuron* **96**, 17–42 (2017).
- 4. Dunn, K. M. & Nelson, M. T. Neurovascular signaling in the brain and the pathological consequences of hypertension. *Am. J. Physiol. Heart. Circ. Physiol.* **306**, H1–H14 (2014).
- Mattson, M. P. & Arumugam, T. V. Hallmarks of brain aging: adaptive and pathological modification by metabolic states. Cell Metab. 27, 1176–1199 (2018).
- Lucin, K. M. & Wyss-Coray, T. Immune activation in brain aging and neurodegeneration: too much or too little? *Neuron* 64, 110–122 (2009)
- Sweeney, M. D., Sagare, A. P. & Zlokovic, B. V. Blood-brain barrier breakdown in Alzheimer disease and other neurodegenerative disorders. *Nat. Rev. Neurol.* 14, 133–150 (2018).
- 8. Jia, G., Aroor, A. R., Jia, C. & Sowers, J. R. Endothelial cell senescence in aging-related vascular dysfunction. *Biochim. Biophys. Acta Mol. Basis Dis.* **1865**, 1802–1809 (2019).
- Ungvari, Z. et al. Endothelial dysfunction and angiogenesis impairment in the ageing vasculature. *Nat. Rev. Cardiol.* 15, 555–565 (2018).
- Donato, A. J., Machin, D. R. & Lesniewski, L. A. Mechanisms of dysfunction in the aging vasculature and role in age-related disease. Circ. Res. 123, 825–848 (2018).
- Graves, S. I. & Baker, D. J. Implicating endothelial cell senescence to dysfunction in the ageing and diseased brain. *Basic Clin. Pharmacol. Toxicol.* 127, 102–110 (2020).
- Costea, L. et al. The blood-brain barrier and its intercellular junctions in age-related brain disorders. *Int. J. Mol. Sci.* 20, 5472 (2019).
- Goodall, E. F. et al. Age-associated changes in the blood-brain barrier: comparative studies in human and mouse. *Neuropathol. Appl. Neurobiol.* 44, 328–340 (2018).
- Banks, W. A., Reed, M. J., Logsdon, A. F., Rhea, E. M. & Erickson, M. A. Healthy aging and the blood-brain barrier. *Nat. Aging* 1, 243–254 (2021).
- Tarantini, S., Tran, C. H. T., Gordon, G. R., Ungvari, Z. & Csiszar, A. Impaired neurovascular coupling in aging and Alzheimer's disease: contribution of astrocyte dysfunction and endothelial impairment to cognitive decline. Exp. Gerontol. 94, 52–58 (2017).
- Tarumi, T. & Zhang, R. Cerebral blood flow in normal aging adults: cardiovascular determinants, clinical implications, and aerobic fitness. J. Neurochem. 144, 595–608 (2018).
- 17. Brandes, R. P., Fleming, I. & Busse, R. Endothelial aging. *Cardiovasc. Res.* **66**, 286–294 (2005).
- Donato, A. J., Morgan, R. G., Walker, A. E. & Lesniewski, L. A. Cellular and molecular biology of aging endothelial cells. J. Mol. Cell. Cardiol. 89, 122–135 (2015).

- Di Micco, R., Krizhanovsky, V., Baker, D. & d'Adda di Fagagna, F. Cellular senescence in ageing: from mechanisms to therapeutic opportunities. Nat. Rev. Mol. Cell Biol. 22, 75–95 (2021).
- Slack, R. J., Macdonald, S. J. F., Roper, J. A., Jenkins, R. G. & Hatley, R. J. D. Emerging therapeutic opportunities for integrin inhibitors. *Nat. Rev. Drug Discov.* 21, 60–78 (2021).
- Shin, E. Y. et al. Integrin-mediated adhesions in regulation of cellular senescence. Sci. Adv. 6, eaay3909 (2020).
- Hafezi-Moghadam, A., Thomas, K. L. & Wagner, D. D. ApoE deficiency leads to a progressive age-dependent blood-brain barrier leakage.
 Am. J. Physiol. Cell Physiol. 292, C1256–C1262 (2007).
- Bell, R. D. et al. Apolipoprotein E controls cerebrovascular integrity via cyclophilin A. Nature 485, 512–516 (2012).
- Migrino, R. Q. et al. Amyloidogenic medin induces endothelial dysfunction and vascular inflammation through the receptor for advanced glycation endproducts. *Cardiovasc. Res.* 113, 1389–1402 (2017).
- Degenhardt, K. et al. Medin aggregation causes cerebrovascular dysfunction in aging wild-type mice. Proc. Natl Acad. Sci. USA 117, 23925–23931 (2020).
- Migrino, R. Q. et al. Cerebrovascular medin is associated with Alzheimer's disease and vascular dementia. Alzheimers Dement. (Amst.) 12, e12072 (2020).
- Tabula Muris, C. A single-cell transcriptomic atlas characterizes ageing tissues in the mouse. *Nature* 583, 590–595 (2020).
- Ximerakis, M. et al. Single-cell transcriptomic profiling of the aging mouse brain. Nat. Neurosci. 22, 1696–1708 (2019).
- Angelidis, I. et al. An atlas of the aging lung mapped by single cell transcriptomics and deep tissue proteomics. *Nat. Commun.* 10, 963 (2019).
- Yang, A. C. et al. Physiological blood-brain transport is impaired with age by a shift in transcytosis. Nature 583, 425-430 (2020).
- Chen, M. B. et al. Brain endothelial cells are exquisite sensors of age-related circulatory cues. Cell Rep. 30, 4418–4432 e4414 (2020).
- Zhao, L. et al. Pharmacologically reversible zonation-dependent endothelial cell transcriptomic changes with neurodegenerative disease associations in the aged brain. *Nat. Commun.* 11, 4413 (2020).
- Aldridge, S. & Teichmann, S. A. Single cell transcriptomics comes of age. Nat. Commun. 11. 4307 (2020).
- 34. Carlyle, B. C. et al. A multiregional proteomic survey of the postnatal human brain. *Nat. Neurosci.* **20**, 1787–1795 (2017).
- Maier, T., Guell, M. & Serrano, L. Correlation of mRNA and protein in complex biological samples. FEBS Lett. 583, 3966–3973 (2009).
- de Sousa Abreu, R., Penalva, L. O., Marcotte, E. M. & Vogel, C. Global signatures of protein and mRNA expression levels. *Mol. Biosyst.* 5, 1512–1526 (2009).
- 37. Vogel, C. & Marcotte, E. M. Insights into the regulation of protein abundance from proteomic and transcriptomic analyses. *Nat. Rev. Genet.* **13**, 227–232 (2012).
- Wang, D. et al. A deep proteome and transcriptome abundance atlas of 29 healthy human tissues. Mol. Syst. Biol. 15, e8503 (2019).
- 39. McDowell, I. C. et al. Clustering gene expression time series data using an infinite Gaussian process mixture model. *PLoS Comput. Biol.* **14**, e1005896 (2018).
- Rayon, T. et al. Species-specific pace of development is associated with differences in protein stability. Science 369, eaba7667 (2020).
- Kim, D. S. et al. The dynamic, combinatorial cis-regulatory lexicon of epidermal differentiation. Nat. Genet. 53, 1564–1576 (2021).
- 42. Shcherbina, A. et al. Dissecting murine muscle stem cell aging through regeneration using integrative genomic analysis. *Cell Rep.* **32**, 107964 (2020).

- 43. Garcia-Cabezas, M. A., John, Y. J., Barbas, H. & Zikopoulos, B. Distinction of neurons, glia and endothelial cells in the cerebral cortex: an algorithm based on cytological features. *Front. Neuroanat.* **10**, 107 (2016).
- 44. Bjørnholm, K. D. et al. A robust and efficient microvascular isolation method for multimodal characterization of the mouse brain vasculature. *Cell Rep. Methods* **3**, 100431 (2023).
- Yousef, H. et al. Aged blood impairs hippocampal neural precursor activity and activates microglia via brain endothelial cell VCAM1. Nat. Med. 25, 988–1000 (2019).
- Schaum, N. et al. Ageing hallmarks exhibit organ-specific temporal signatures. *Nature* 583, 596–602 (2020).
- Zhou, T. et al. Microvascular endothelial cells engulf myelin debris and promote macrophage recruitment and fibrosis after neural injury. Nat. Neurosci. 22, 421–435 (2019).
- 48. Safaiyan, S. et al. Age-related myelin degradation burdens the clearance function of microglia during aging. *Nat. Neurosci.* **19**, 995–998 (2016).
- 49. Khalil, M. et al. Serum neurofilament light levels in normal aging and their association with morphologic brain changes. *Nat. Commun.* **11**, 812 (2020).
- Eisen, M. B., Spellman, P. T., Brown, P. O. & Botstein, D. Cluster analysis and display of genome-wide expression patterns. *Proc. Natl Acad. Sci. USA* 95, 14863–14868 (1998).
- Chen, Z. et al. Reciprocal regulation of eNOS and caveolin-1 functions in endothelial cells. *Mol. Biol. Cell* 29, 1190–1202 (2018).
- D'Souza-Schorey, C. & Chavrier, P. ARF proteins: roles in membrane traffic and beyond. *Nat. Rev. Mol. Cell Biol.* 7, 347–358 (2006).
- Donaldson, J. G. Multiple roles for Arf6: sorting, structuring, and signaling at the plasma membrane. J. Biol. Chem. 278, 41573–41576 (2003).
- Schweitzer, J. K. & D'Souza-Schorey, C. A requirement for ARF6 during the completion of cytokinesis. *Exp. Cell. Res.* 311, 74–83 (2005).
- 55. Korbelin, J. et al. A brain microvasculature endothelial cell-specific viral vector with the potential to treat neurovascular and neurological diseases. *EMBO Mol. Med.* **8**, 609–625 (2016).
- 56. Govindpani, K. et al. Vascular dysfunction in Alzheimer's disease: a prelude to the pathological process or a consequence of it?

 J. Clin. Med. 8, 651 (2019).
- Malek, N. et al. Vascular disease and vascular risk factors in relation to motor features and cognition in early Parkinson's disease. Mov. Disord. 31, 1518–1526 (2016).
- 58. ladecola, C. The pathobiology of vascular dementia. *Neuron* **80**, 844–866 (2013).
- Cohen, R. M., Small, C., Lalonde, F., Friz, J. & Sunderland, T. Effect of apolipoprotein E genotype on hippocampal volume loss in aging healthy women. *Neurology* 57, 2223–2228 (2001).
- Espeseth, T. et al. Accelerated age-related cortical thinning in healthy carriers of apolipoprotein E ε4. Neurobiol. Aging 29, 329–340 (2008).
- 61. Love, S. et al. Premorbid effects of APOE on synaptic proteins in human temporal neocortex. *Neurobiol. Aging* **27**, 797–803 (2006).
- 62. den Heijer, T. et al. Hippocampal, amygdalar, and global brain atrophy in different apolipoprotein E genotypes. *Neurology* **59**, 746–748 (2002).
- Laursen, J. B. et al. Endothelial regulation of vasomotion in apoE-deficient mice: implications for interactions between peroxynitrite and tetrahydrobiopterin. *Circulation* 103, 1282–1288 (2001).
- 64. d'Uscio, L. V. et al. Mechanism of endothelial dysfunction in apolipoprotein E-deficient mice. *Arterioscler. Thromb. Vasc. Biol.* **21**, 1017–1022 (2001).

- Ohashi, M., Runge, M. S., Faraci, F. M. & Heistad, D. D. MnSOD deficiency increases endothelial dysfunction in ApoE-deficient mice. Arterioscler. Thromb. Vasc. Biol. 26, 2331–2336 (2006).
- Van Acker, T., Tavernier, J. & Peelman, F. The small GTPase Arf6: an overview of its mechanisms of action and of its role in hostpathogen interactions and innate immunity. *Int. J. Mol. Sci.* 20, 2209 (2019).
- Palacios, F., Price, L., Schweitzer, J., Collard, J. G. & D'Souza-Schorey, C. An essential role for ARF6-regulated membrane traffic in adherens junction turnover and epithelial cell migration. *EMBO J.* 20, 4973–4986 (2001).
- D'Souza-Schorey, C., Li, G., Colombo, M. I. & Stahl, P. D. A regulatory role for ARF6 in receptor-mediated endocytosis. Science 267, 1175–1178 (1995).
- Song, L. & Pachter, J. S. Monocyte chemoattractant protein-1 alters expression of tight junction-associated proteins in brain microvascular endothelial cells. *Microvasc. Res.* 67, 78–89 (2004).
- Crewe, C. et al. An endothelial-to-adipocyte extracellular vesicle axis governed by metabolic state. Cell 175, 695–708 (2018).
- Mathiesen, A. et al. Endothelial extracellular vesicles: from keepers of health to messengers of disease. *Int. J. Mol. Sci.* 22, 4640 (2021).
- Blackburn, J. B., D'Souza, Z. & Lupashin, V. V. Maintaining order: COG complex controls Golgi trafficking, processing, and sorting. FEBS Lett. 593, 2466–2487 (2019).
- Wagner, J. et al. Overexpression of the novel senescence marker β-galactosidase (GLB1) in prostate cancer predicts reduced PSA recurrence. PLoS ONE 10, e0124366 (2015).
- Debacq-Chainiaux, F., Erusalimsky, J. D., Campisi, J. & Toussaint, O. Protocols to detect senescence-associated beta-galactosidase (SA-βgal) activity, a biomarker of senescent cells in culture and in vivo. *Nat. Protoc.* 4, 1798–1806 (2009).
- Hipp, M. S., Kasturi, P. & Hartl, F. U. The proteostasis network and its decline in ageing. Nat. Rev. Mol. Cell Biol. 20, 421–435 (2019).
- Wan, B. et al. GIT1 protects traumatically injured spinal cord by prompting microvascular endothelial cells to clear myelin debris. Aging (Albany NY) 13, 7067–7083 (2021).
- Johnsen, K. B., Burkhart, A., Thomsen, L. B., Andresen, T. L. & Moos, T. Targeting the transferrin receptor for brain drug delivery. *Prog. Neurobiol.* 181, 101665 (2019).
- Terstappen, G. C., Meyer, A. H., Bell, R. D. & Zhang, W. Strategies for delivering therapeutics across the blood-brain barrier. Nat. Rev. Drug Discov. 20, 362–383 (2021).
- Okuyama, T. et al. Iduronate-2-sulfatase with anti-human transferrin receptor antibody for neuropathic mucopolysaccharidosis II: a phase 1/2 trial. Mol. Ther. 27, 456–464 (2019).
- Kariolis, M. S. et al. Brain delivery of therapeutic proteins using an Fc fragment blood-brain barrier transport vehicle in mice and monkeys. Sci. Transl. Med. 12, eaay1359 (2020).
- Humphries, J. D., Byron, A. & Humphries, M. J. Integrin ligands at a glance. J. Cell Sci. 119, 3901–3903 (2006).
- 82. Smith, J. W., Ruggeri, Z. M., Kunicki, T. J. & Cheresh, D. A. Interaction of integrins $\alpha_{\nu}\beta_{3}$ and glycoprotein IIb-IIIa with fibrinogen. Differential peptide recognition accounts for distinct binding sites. *J. Biol. Chem.* **265**, 12267–12271 (1990).
- 83. Silvestre, J. S. et al. Lactadherin promotes VEGF-dependent neovascularization. *Nat. Med.* **11**, 499–506 (2005).
- 84. Marazuela, P. et al. MFG-E8 (LACTADHERIN): a novel marker associated with cerebral amyloid angiopathy. *Acta Neuropathol. Commun.* **9**, 154 (2021).
- Vanlandewijck, M. et al. Author Correction: A molecular atlas of cell types and zonation in the brain vasculature. *Nature* 560, E3 (2018).
- 86. Hanayama, R. et al. Identification of a factor that links apoptotic cells to phagocytes. *Nature* **417**, 182–187 (2002).

- 87. Tai, L. M. et al. The role of *APOE* in cerebrovascular dysfunction. *Acta Neuropathol.* **131**. 709–723 (2016).
- Yang, A. C. et al. A human brain vascular atlas reveals diverse cell mediators of Alzheimeras disease risk. *Nature* 603, 885–892 (2022).
- 89. Halliday, M. R. et al. Accelerated pericyte degeneration and blood-brain barrier breakdown in apolipoprotein E4 carriers with Alzheimer's disease. *J. Cereb. Blood Flow Metab.* **36**, 216–227 (2016).
- Carvalho, C. & Moreira, P. I. Oxidative stress: a major player in cerebrovascular alterations associated to neurodegenerative events. Front. Physiol. 9, 806 (2018).
- 91. Finkel, T. & Holbrook, N. J. Oxidants, oxidative stress and the biology of ageing. *Nature* **408**, 239–247 (2000).
- Johnson, A. A. & Stolzing, A. The role of lipid metabolism in aging, lifespan regulation, and age-related disease. *Aging Cell* 18, e13048 (2019).
- 93. Bazzoni, G. & Dejana, E. Endothelial cell-to-cell junctions: molecular organization and role in vascular homeostasis. *Physiol. Rev.* **84**, 869–901 (2004).
- 94. Xiao, K. et al. p120-catenin regulates clathrin-dependent endocytosis of VE-cadherin. *Mol. Biol. Cell* **16**, 5141–5151 (2005).
- Iyer, S., Ferreri, D. M., DeCocco, N. C., Minnear, F. L. & Vincent, P. A. VE-cadherin-p120 interaction is required for maintenance of endothelial barrier function. *Am. J. Physiol. Lung Cell. Mol. Physiol.* 286, L1143–L1153 (2004).
- 96. Armulik, A. et al. Pericytes regulate the blood-brain barrier. *Nature* **468**, 557–561 (2010).
- 97. Daneman, R. et al. The mouse blood-brain barrier transcriptome: a new resource for understanding the development and function of brain endothelial cells. *PLoS ONE* **5**, e13741 (2010).
- 98. Diz, A. P., Truebano, M. & Skibinski, D. O. F. The consequences of sample pooling in proteomics: an empirical study. *Electrophoresis* **30**, 2967–2975 (2009).
- 99. Jang, S., Collin de l'Hortet, A. & Soto-Gutierrez, A. Induced pluripotent stem cell-derived endothelial cells: overview, current advances, applications, and future directions. *Am. J. Pathol.* **189**, 502–512 (2019).
- 100. Marquer, C. et al. Arf6 controls retromer traffic and intracellular cholesterol distribution via a phosphoinositide-based mechanism. Nat. Commun. 7, 11919 (2016).
- Sorensen, I., Adams, R. H. & Gossler, A. DLL1-mediated Notch activation regulates endothelial identity in mouse fetal arteries. *Blood* 113, 5680–5688 (2009).
- 102. Monet-Lepretre, M. et al. Abnormal recruitment of extracellular matrix proteins by excess Notch3 ECD: a new pathomechanism in CADASIL. *Brain* **136**, 1830–1845 (2013).
- 103. Zellner, A. et al. CADASIL brain vessels show a HTRA1 loss-of-function profile. *Acta Neuropathol.* **136**, 111–125 (2018).
- 104. Hughes, C. S. et al. Single-pot, solid-phase-enhanced sample preparation for proteomics experiments. *Nat. Protoc.* 14, 68–85 (2019).
- 105. Cox, J. et al. Accurate proteome-wide label-free quantification by delayed normalization and maximal peptide ratio extraction, termed MaxLFQ. Mol. Cell. Proteomics 13, 2513–2526 (2014).
- 106. Sinitcyn, P. et al. MaxDIA enables library-based and library-free data-independent acquisition proteomics. *Nat. Biotechnol.* 39, 1563–1573 (2021).
- Demichev, V., Messner, C. B., Vernardis, S. I., Lilley, K. S. & Ralser, M. DIA-NN: neural networks and interference correction enable deep proteome coverage in high throughput. *Nat. Methods* 17, 41–44 (2020).
- 108. Tusher, V. G., Tibshirani, R. & Chu, G. Significance analysis of microarrays applied to the ionizing radiation response. *Proc. Natl Acad. Sci. USA* 98, 5116–5121 (2001).

- 109. Jiao, X. et al. DAVID-WS: a stateful web service to facilitate gene/protein list analysis. *Bioinformatics* **28**, 1805–1806 (2012).
- Liao, Y., Wang, J., Jaehnig, E. J., Shi, Z. & Zhang, B. WebGestalt 2019: gene set analysis toolkit with revamped UIs and APIs. Nucleic Acids Res. 47, W199–W205 (2019).
- Jourquin, J., Duncan, D., Shi, Z. & Zhang, B. GLAD4U: deriving and prioritizing gene lists from PubMed literature. *BMC Genomics* 13, S20 (2012).
- 112. Schmid, B. et al. Generation of a set of isogenic, gene-edited iPSC lines homozygous for all main APOE variants and an APOE knock-out line. Stem Cell Res. 34, 101349 (2019).
- Paquet, D. et al. Efficient introduction of specific homozygous and heterozygous mutations using CRISPR/Cas9. *Nature* 533, 125–129 (2016).
- 114. Kwart, D., Paquet, D., Teo, S. & Tessier-Lavigne, M. Precise and efficient scarless genome editing in stem cells using CORRECT. *Nat. Protoc.* **12**, 329–354 (2017).
- 115. Steyer, B., Cory, E. & Saha, K. Developing precision medicine using scarless genome editing of human pluripotent stem cells. *Drug Discov. Today Technol.* **28**, 3–12 (2018).
- Skarnes, W. C., Pellegrino, E. & McDonough, J. A. Improving homology-directed repair efficiency in human stem cells. *Methods* 164-165, 18–28 (2019).
- Concordet, J. P. & Haeussler, M. CRISPOR: intuitive guide selection for CRISPR/Cas9 genome editing experiments and screens. *Nucleic Acids Res.* 46, W242–W245 (2018).
- Weisheit, I. et al. Simple and reliable detection of CRISPR-induced on-target effects by qgPCR and SNP genotyping. *Nat. Protoc.* 16, 1714–1739 (2021).
- 119. Moorhead, A. M., Jung, J. Y., Smirnov, A., Kaufer, S. & Scidmore, M. A. Multiple host proteins that function in phosphatidylinositol-4-phosphate metabolism are recruited to the chlamydial inclusion. *Infect. Immun.* 78, 1990–2007 (2010).
- 120. Challis, R. C. et al. Systemic AAV vectors for widespread and targeted gene delivery in rodents. *Nat. Protoc.* **14**, 379–414 (2019).
- Xiao, X., Li, J. & Samulski, R. J. Production of high-titer recombinant adeno-associated virus vectors in the absence of helper adenovirus. J. Virol. 72, 2224–2232 (1998).
- 122. Kislinger, G. et al. Multiscale ATUM-FIB microscopy enables targeted ultrastructural analysis at isotropic resolution. *iScience* **23**, 101290 (2020).
- 123. Perez-Riverol, Y. et al. The PRIDE database resources in 2022: a hub for mass spectrometry-based proteomics evidences. *Nucleic Acids Res.* **50**, D543–D552 (2022).

Acknowledgements

We thank T. Webb for technical advice for the endothelial cell differentiation protocol; Y. Asare and U. Schillinger for help with the AAV injection; and B. Lindner, A. Berghofer, L. Peischer, M. Schneider and A. Nottebrock for technical assistance. This study received funding from the European Union's Horizon 2020 Research and Innovation Program SVDs@target (no. 666881, to M.D.); the European Innovation Council program (grant agreement no. 101115381, to M.D.);

the Deutsche Forschungsgemeinschaft (DFG), as part of the Munich Cluster for Systems Neurology (SyNergy; EXC 2145 SyNergy – ID 390857198, to M.D.), and individual project grants (DI 722/13-1; DI 722/16-1 and BE 6169/1-1, to M.D.); the Vascular Dementia Research Foundation, through the Federal Ministry for Education and Research (BMBF, CLINSPECT-M, to M.D.); a grant from the Leducq Foundation (grant agreement N022CVD01, to M.D.); ERA-NET Neuron (MatriSVDs, to M.D.); and the LMUexcellent fund (to M.D.). Graphics from Figs. 1a, 3a,b and 4a,e were created with Biorender.

Author contributions

K.T.V., J.G.G. and M.D. designed the project. S.A.M. and A.S. performed mass spectrometry. K.T.V., R.M. and N.B. analyzed proteomics experiments. K.T.V. and J.G.G. performed and analyzed biochemical and immunocytochemistry experiments. J.G.G., D.C. and S.R. performed gene editing and analyzed cell culture experiments. M.S. performed electron microscopy. M.I.T. designed and established the publicly available database. J.K. provided AAV-BR1 and F.B. produced Arf6-AAV for the in vivo experiments. M.D., S.L., D.P., M.S., C.H. and A.E. supervised the experiments. K.T.V., J.G.G. and M.D. wrote the manuscript. All authors read and revised the manuscript.

Competing interests

The authors declare no competing interests.

Additional information

Extended data is available for this paper at https://doi.org/10.1038/s43587-024-00598-z.

Supplementary information The online version contains supplementary material available at https://doi.org/10.1038/s43587-024-00598-z.

Correspondence and requests for materials should be addressed to Katalin Todorov-Völgyi or Martin Dichgans.

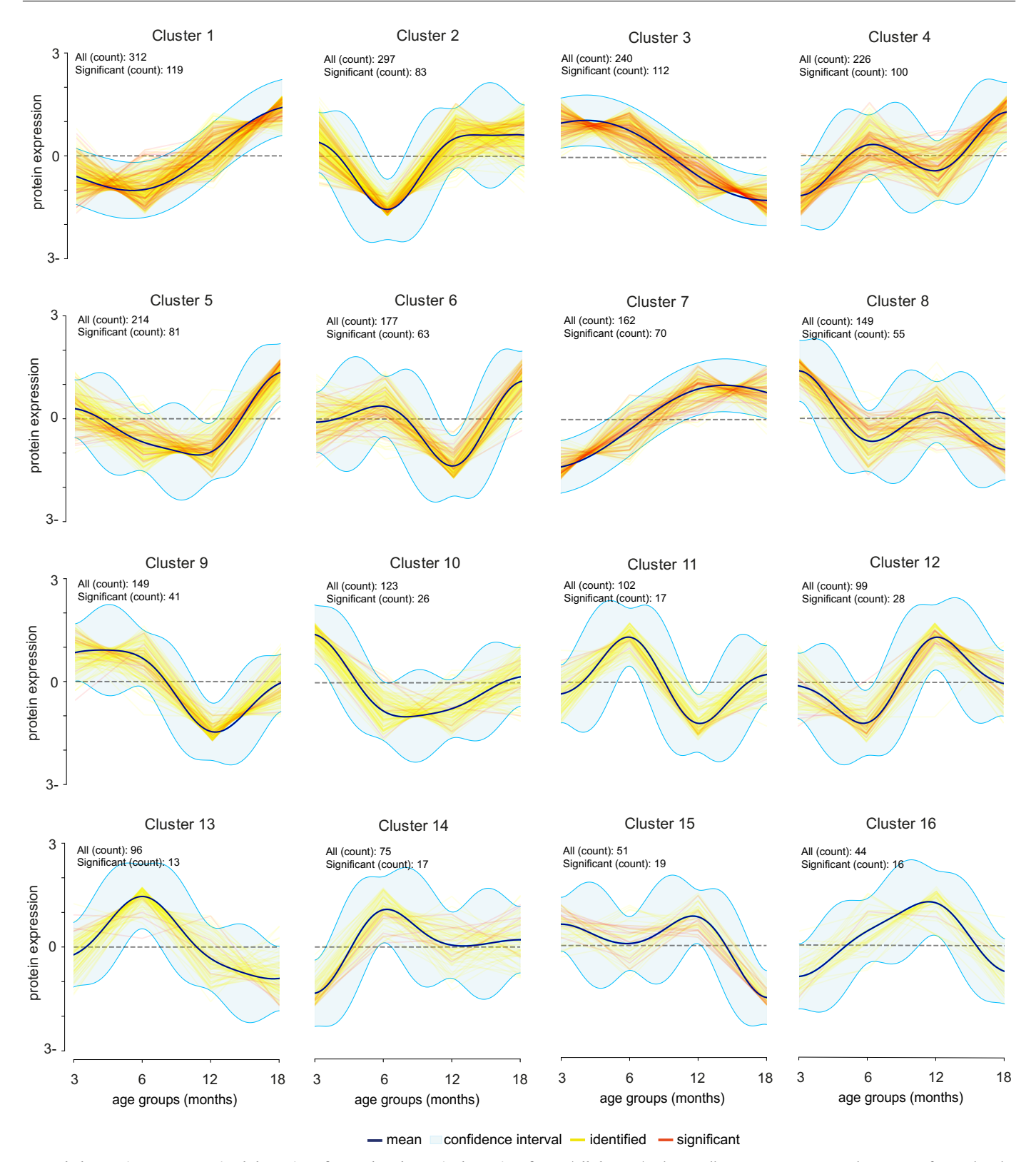
Peer review information *Nature Aging* thanks the anonymous reviewers for their contribution to the peer review of this work.

Reprints and permissions information is available at www.nature.com/reprints.

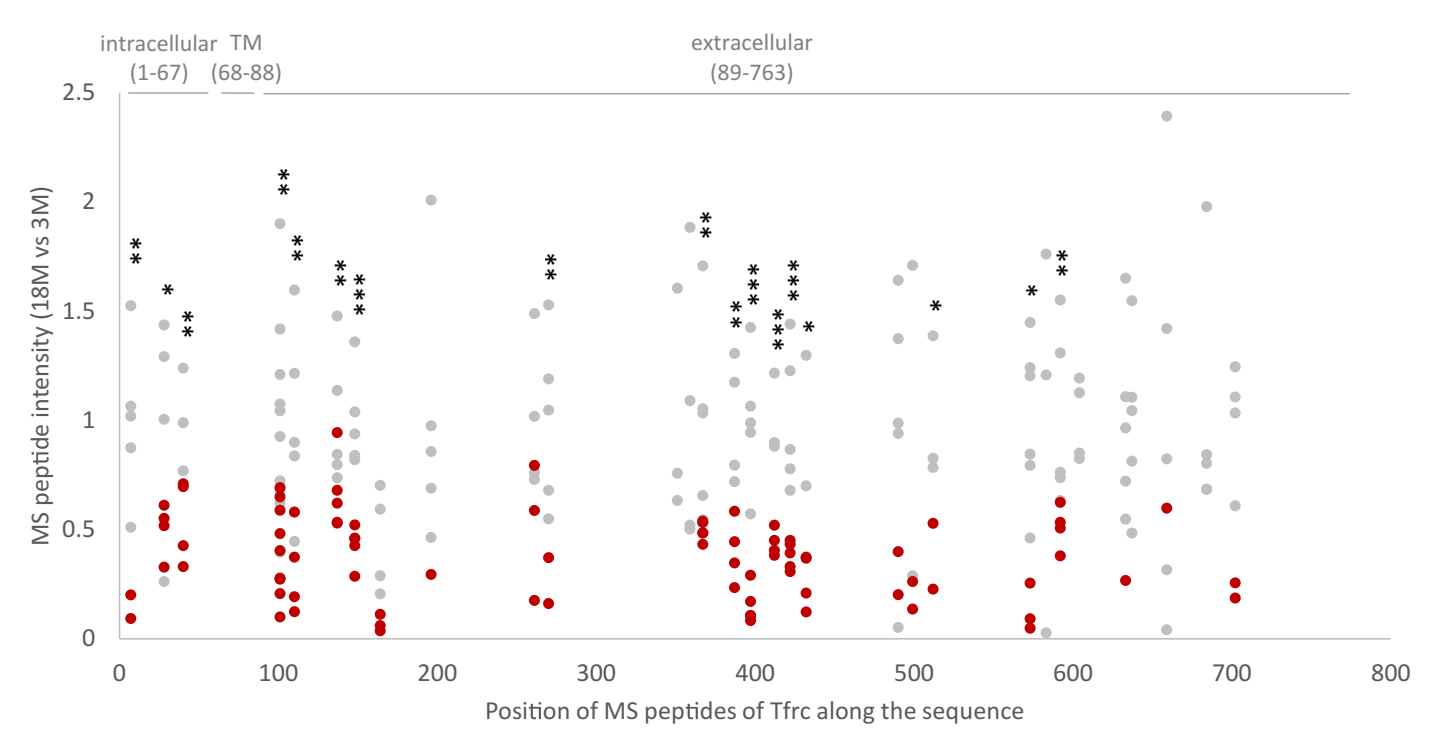
Publisher's note Springer Nature remains neutral with regard to jurisdictional claims in published maps and institutional affiliations.

Springer Nature or its licensor (e.g. a society or other partner) holds exclusive rights to this article under a publishing agreement with the author(s) or other rightsholder(s); author self-archiving of the accepted manuscript version of this article is solely governed by the terms of such publishing agreement and applicable law.

© The Author(s), under exclusive licence to Springer Nature America, Inc. 2024



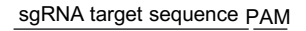
Extended Data Fig. 1 | Unsupervised clustering of age-related protein dynamics of BECs (all clusters). Clusters illustrating variations in the pattern of age-related protein abundance changes. (Blue line: cluster mean, light blue band: confidence interval, yellow line: all quantified, red line: significant protein abundance in each cluster).



 $\label{lem:condition} \textbf{Extended Data Fig. 2} \ | \ \textbf{Mass spectrometry-based analysis of region-specific changes in Tfrc levels.} \ Following proteomic analysis of BECs from 18-vs 3-month-old mice, the signal intensity of Tfrc-related tryptic peptides was mapped onto the protein sequence. The mean intensity in samples from 1.500×10^{-5} and 1.500×10^{-5} are the sequence of the protein sequence. The mean intensity in samples from 1.500×10^{-5} are the sequence of the protein sequence. The mean intensity in samples from 1.500×10^{-5} are the sequence of the protein sequence of the$

3-month-old mice was set to 1. Significance was tested by Student´s t-test. The intracellular (aa 1-67), transmembrane (aa 68-88) and extracellular (aa 89-763) regions of Tfrc are labeled.

Α



...aacaaggaaatgcggatcctcatgttgggcctggacggcggcaagacaacaatcctgtacaagttgaagctgggccagtcggtgacc...

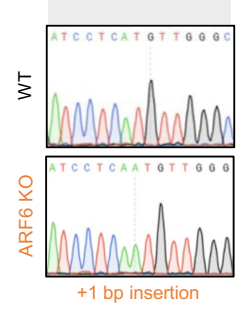
Exon 2

Asn Lys Glu Met Arg lle Leu Met Leu Gly Leu Asp Ala Ala Gly Lys Thr Thr lle Leu Tyr Lys Leu Lys Leu Gly Gln Ser Val Thr

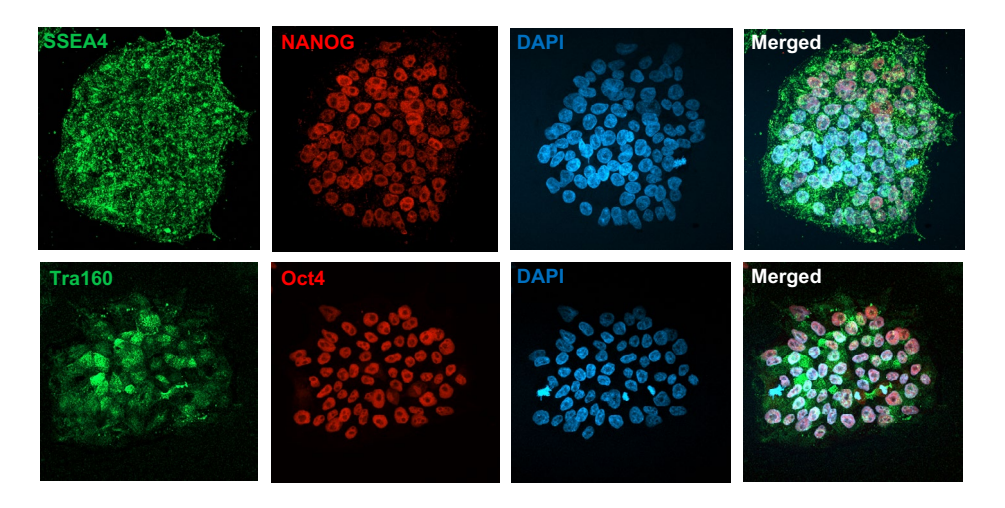
Cys Trp Ala Trp Thr Arg Pro Ala Arg Gln Gln Ser Cys Thr Ser * Ser Trp Ala Ser Arg *

Reading frame WT

Reading frame +1bp



В

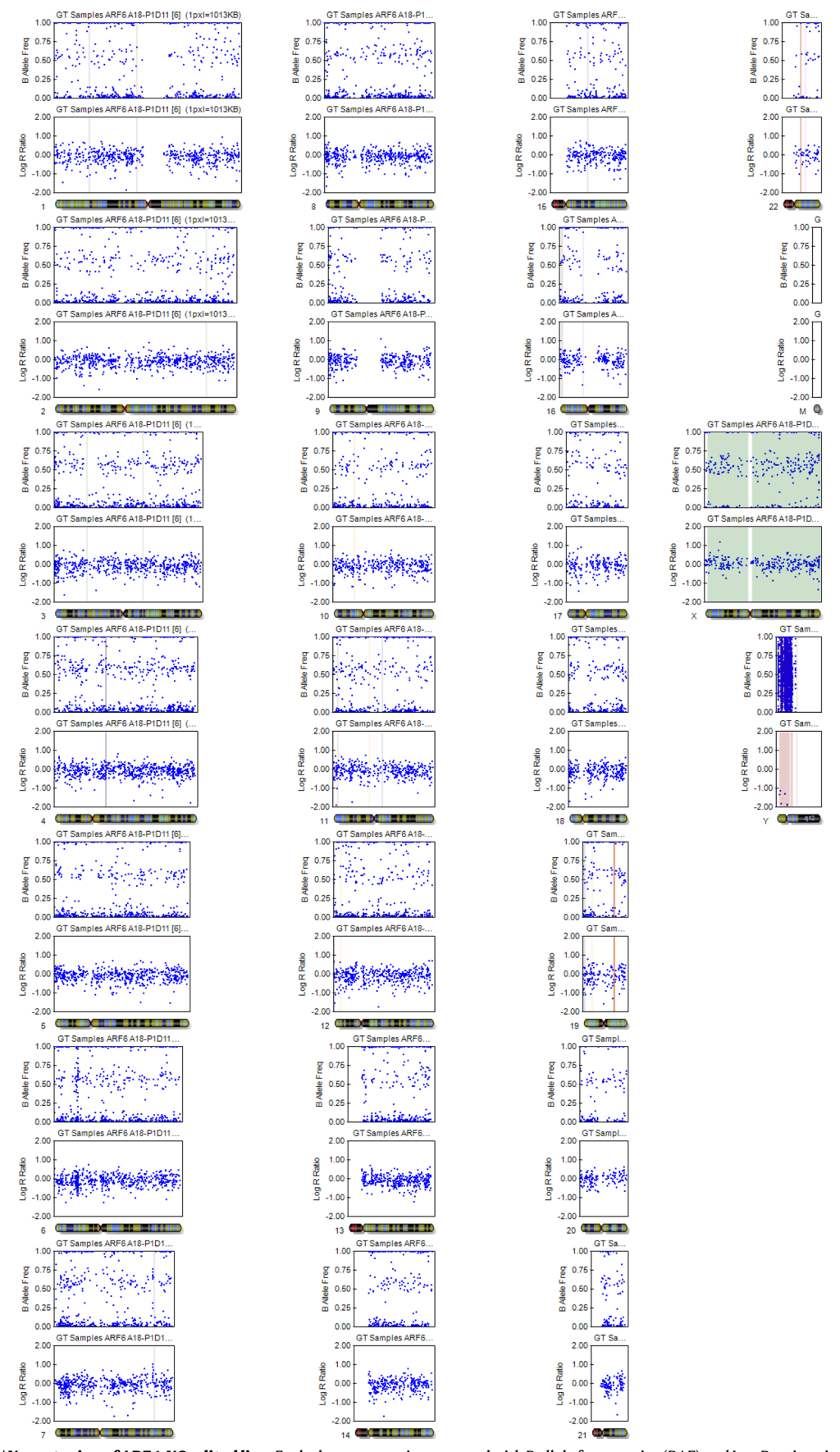


C

Gene	ID	Sequence	M ismatch position	M ismatch Count	M IT score	CFD score	Location	Locus description	Indels detected
ARF6	gRNA	GGAAATGCGGATCCTCATGTTGG	Target		-	-	-	-	-
ARF6	CFD OT 1	GGAAAAATGTATCCTCATGTAGG	*** *	4	0.496624	0.616146	8:134804959:134805481:-1	intergenic:MIR30D-AC083843.2	None
ARF6	CFD OT 2	TGAAATGTAGACCCTCATGTTGG	***	4	0.430092	0.532895	13:36733486:36734008:1	intergenic:AL136160.1-RFXAP	None
ARF6	CFD OT 3	AGAAATGTGGAACTTCATGTGGG	**.**	4	0.110194	0.462	4:78874823:78875345:1	intron:BMP2K	None
ARF6	CFD OT 4	GAAAATGCAGATCCTAATTTCGG	***.	4	0.052415	0.362637	20:5032709:5033231:1	intergenic:SLC23A2-RP5-1116H23.6	None
ARF6	CFD OT 5	GGAAATGTTGATCTTAATGTGGG	** **	4	0.021373	0.342222	13:58747536:58748058:-1	intergenic:RNY4P29-AL359262.1	None
ARF6	MIT OT 1	AGTAGTGAGGATCCTCATGTTGG	****	4	1.345833	0.297318	5:92369914:92370436:-1	intergenic:RP 11-348J24.1-RP 11-348J24.2	None
ARF6	MIT OT 2	GGGAATCGGAATCCTCATGTGGG	.***	4	0.846587	0.252083	1:166974117:166974639:1	intron:ILDR2	None
ARF6	MIT OT 3	AGAGATGGGGTTCCTCATGTTGG	***.	4	0.794051	0.111264	2:233186656:233187178:1	intron:INPP5D	None
ARF6	MIT OT 4	GAAGATGTGGATCCTCATGGTGG	.***	4	0.697447	0.08166	6:27107660:27108182:1	intergenic:TRI-TAT2-2-RNU2-62P	None
ARF6	MIT OT 5	GTAAATGAGAATCCTCATGAGGG	* **	4	0.642349	0.217159	6:5830623:5831145:-1	intergenic:FARS2-RP3-380B8.4	None

Extended Data Fig. 3 | CRISPR/Cas9-mediated genome editing of human iPSCs to ARF6-KO. a. ARF6 knockout strategy: Exon 2 of ARF6 was targeted by an sgRNA (target and PAM sequence shown). After editing, one base pair insertion in each allele was generated, producing a premature stop codon.

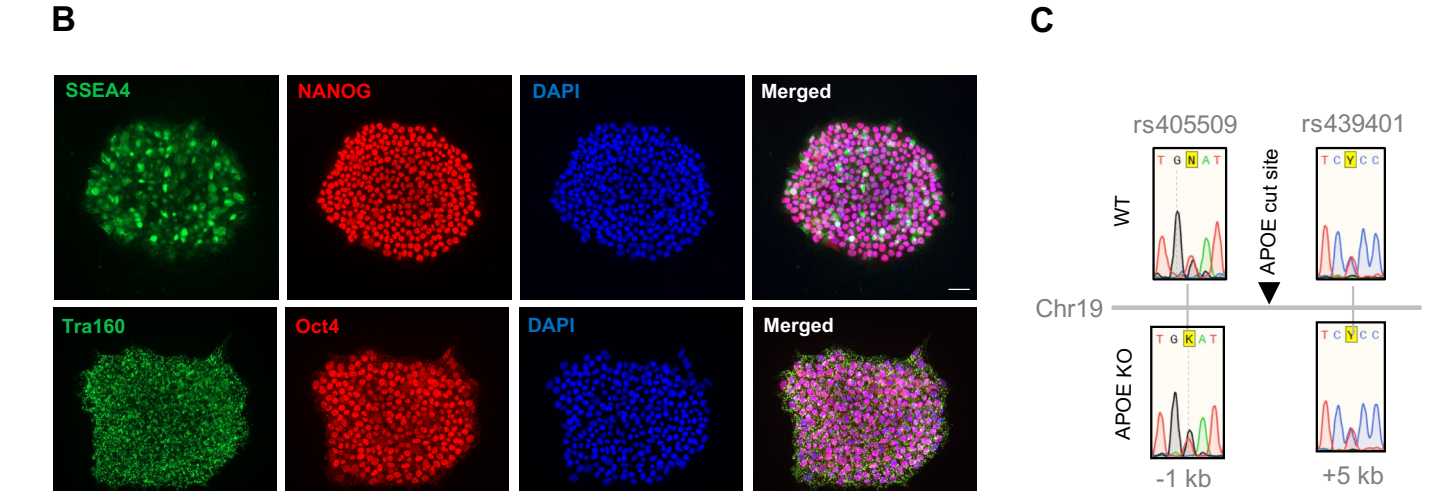
 $\label{eq:b.lmmunofluorescence} b. Immunofluorescence analysis of pluripotency markers, SSEA4, NANOG, TRA160, and OCT 4 with DAPI in ARF6 KO iPSC line. Scale bar 50 <math>\mu$ m. Experiment was repeated 4 times. c. List of top five most similar off-target sites ranked by the CFD and MIT prediction scores. Sanger sequencing detected no off-target editing.



Extended Data Fig. 4 | **Karyotyping of ARF6-KO edited line.** Each chromosome is presented with B allele frequencies (BAF) and Log R rations in the ARF6-KO iPSC line. Blue dots indicate all measured SNPs. For all chromosomes, BAF values indicate normal zygosities and Log R rations the absence of detectable insertions or deletions.





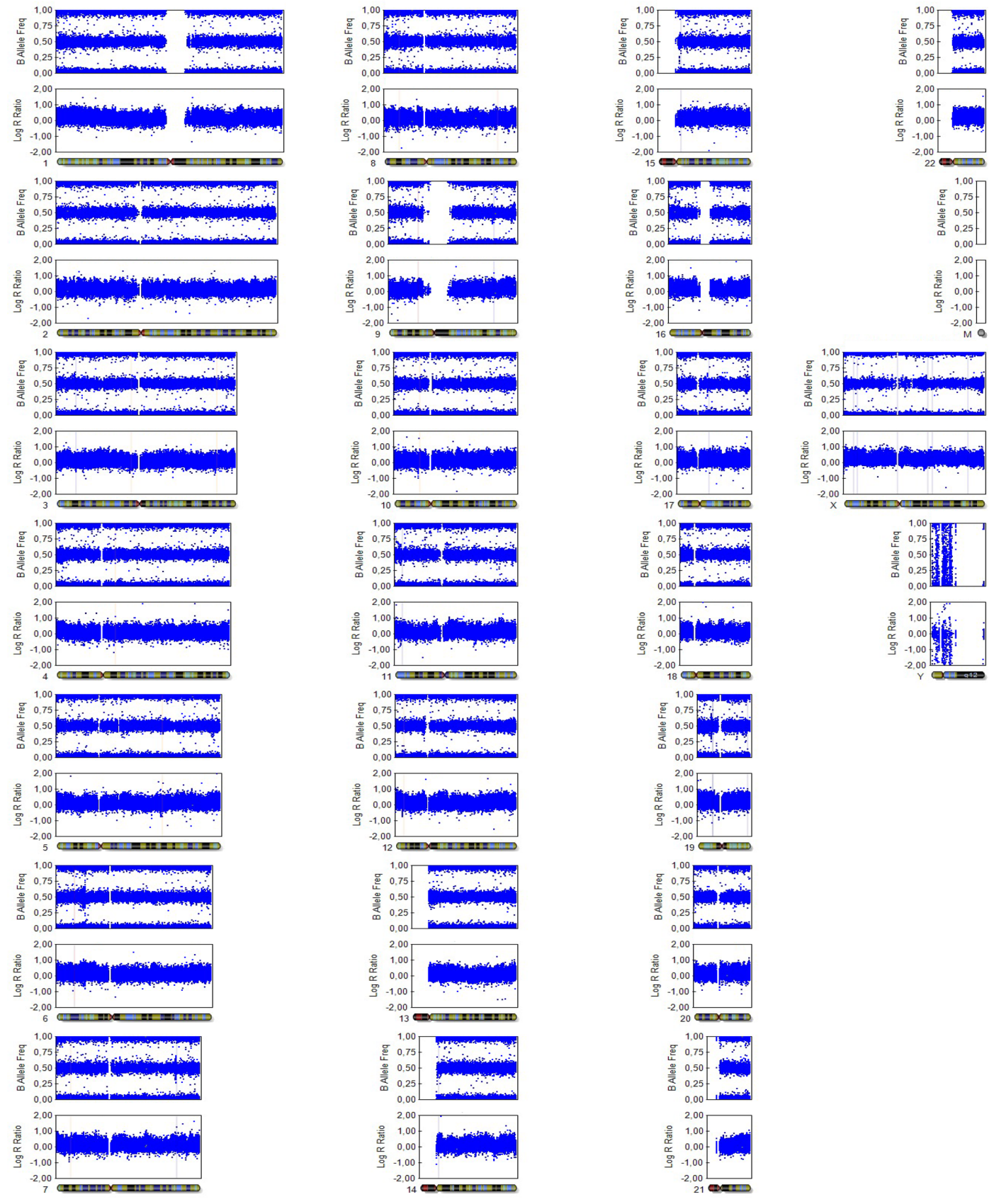


D

Gene	ID	Sequence	Mismatch Position	Mismatch Count	MIT Score	CFD Score	Location	Location Description	Indels detected
APOE	gRNA	GGTTCTGTGGGCTGCGTTGCTGG	Target						
APOE	CFD OT1	AGTTCTGTGGACTCCATTGCAGG	**.**	4	0,023	0,386	4:152072154:152072676:-1	intergenic:RNA5SP169-RP11-18H21.1	None
APOE	CFD OT2	GGTTCTGGGGAATGCGTTTCTGG	*.***.	4	0,123	0,349	13:114048991:114049513:-1	intron:RASA3	None
APOE	CFD OT3	AGTTCAGTTGGCAGCGTTGCAGG	***	4	0,215	0,288	14:101784777:101785299:1	intron:PPP2R5C	None
APOE	MIT OT1	GATTCTGTGGGCTGCGTGGCAGG	.**	2	3,003	0,282	11:116563492:116564014:1	intergenic:AP001891.1-AP000770.2	None
APOE	MIT OT2	GGTTCTTAGAGCTGCGTTGCTGG	**.*	3	1,459	0,427	12:47887516:47888038:-1	intergenic:RP11-89H19.1/VDR-RP11-89H19.1	None
APOE	MIT OT3	CGTTCTGAGGGCTGCCTTGCAGG	**	3	0,542	0	2:46084987:46085509:1	intergenic:AC017006.2-PRKCE	None
APOE	MIT OT4	GGATCTGAGAGCAGCGTTGCTGG	.**.*.	4	0,503	0,369	5:54520000:54520522:1	intron:SNX18	None
APOE	MIT OT5	GGTTCTGTGCTCTGCGGTGCTGG	***	3	0,501	0,018	4:148066707:148067229:1	intron:ARHGAP10	None

Extended Data Fig. 5 | CRISPR/Cas9-mediated genome editing of human iPSCs to APOE-KO. a. APOE knockout strategy: Exon 2 of APOE was targeted by an sgRNA (target and PAM sequence shown), generating a fourteen base pair deletion on one allele and a 13 base pair deletion on the other allele in the APOE KO line. The resulting frameshift exposes a nearby stop codon. **b.** Immunofluorescence analysis of pluripotency markers, SSEA4, NANOG, TRA160, and OCT 4 with

DAPI in APOE KO iPSC line. Scale bar 50 μ m. Experiment was repeated 4 times. **c**. Investigating CRISPR-mediated on-target effects using Sanger sequencing of SNPs near the edited locus in WT and APOE KO iPSC lines showing maintenance of both alleles after editing. **d**. List of top five most similar off-target sites ranked by the CFD and MIT prediction scores, respectively. Sanger sequencing detected no off-target editing.



Extended Data Fig. 6 | Karyotyping of APOE-KO edited line. Analysis of B allele frequencies (BAF) and Log R ratios for all chromosomes in the APOE KO iPSC line. Blue dots indicate all measured SNPs. All chromosomes show the absence of detectable insertions or deletions, showed by Log R ratios, while BAF values indicate for all chromosomes normal zygosities.

nature portfolio

Corresponding author(s):	Martin Dichgans, Katalin Todorov-Völgyi
Last updated by author(s):	Feb 2, 2024

Reporting Summary

Nature Portfolio wishes to improve the reproducibility of the work that we publish. This form provides structure for consistency and transparency in reporting. For further information on Nature Portfolio policies, see our Editorial Policies and the Editorial Policy Checklist.

~				
5	tat	ŀις	ŤΙ.	\sim

For	all statistical analyses, confirm that the following items are present in the figure legend, table legend, main text, or Methods section.
n/a	Confirmed
	The exact sample size (n) for each experimental group/condition, given as a discrete number and unit of measurement
	A statement on whether measurements were taken from distinct samples or whether the same sample was measured repeatedly
	The statistical test(s) used AND whether they are one- or two-sided Only common tests should be described solely by name; describe more complex techniques in the Methods section.
X	A description of all covariates tested
	A description of any assumptions or corrections, such as tests of normality and adjustment for multiple comparisons
	A full description of the statistical parameters including central tendency (e.g. means) or other basic estimates (e.g. regression coefficient) AND variation (e.g. standard deviation) or associated estimates of uncertainty (e.g. confidence intervals)
	For null hypothesis testing, the test statistic (e.g. <i>F</i> , <i>t</i> , <i>r</i>) with confidence intervals, effect sizes, degrees of freedom and <i>P</i> value noted <i>Give P values as exact values whenever suitable.</i>
\times	For Bayesian analysis, information on the choice of priors and Markov chain Monte Carlo settings
\boxtimes	For hierarchical and complex designs, identification of the appropriate level for tests and full reporting of outcomes
	Estimates of effect sizes (e.g. Cohen's d , Pearson's r), indicating how they were calculated
	Our web collection on statistics for higherists contains articles on many of the points above

Software and code

Policy information about availability of computer code

Data collection

For confocal imaging: Zeiss Confocal microscope (LSM800, Zeiss, 40x objective with Airy-scan detector), for Electron Microscopy: JEM 1400plus (JEOL) using the EMplified software (TVIPS, v 0.5.10), for Mass Spectrometry: nanoLC system (EASY-nLC 1200, Thermo Scientific, US) coupled online via a nanospray flex ion source (Proxeon – part of Thermo Scientific, US) equipped with a PRSO-V2 column oven (Sonation, Germany) to a Q-Exactive HF mass spectrometer (Thermo Scientific, US).

Data analysis

We used Maxquant (version 1.6.3.4, or 2.0.1.0) for proteomic data analysis and statistics; STRING (version 11.0) and Cytoscape (version 3.8.2) for protein network representation; ImageJ/Fiji (version 1.52p) for image processing and quantification; Excel (2016) and GraphPad (8.3.1) for additional data analysis, statistics and figure representation.

For manuscripts utilizing custom algorithms or software that are central to the research but not yet described in published literature, software must be made available to editors and reviewers. We strongly encourage code deposition in a community repository (e.g. GitHub). See the Nature Portfolio guidelines for submitting code & software for further information.

Data

Policy information about availability of data

All manuscripts must include a data availability statement. This statement should provide the following information, where applicable:

- Accession codes, unique identifiers, or web links for publicly available datasets
- A description of any restrictions on data availability
- For clinical datasets or third party data, please ensure that the statement adheres to our policy

All mass spectrometry proteomics data have been deposited to the ProteomeXchange Consortium via the PRIDE109 partner repository with the dataset identifiers Project accession: PXD045026 (Username: reviewer_pxd045026@ebi.ac.uk, Password: m4xYRerT); Project accession: PXD045006 (Username: reviewer_pxd045006@ebi.ac.uk, Password: lxbz6JxR); Project accession: PXD045004 (Username: reviewer_pxd045004@ebi.ac.uk, Password: eWml0Cei); Project accession: PXD044996 (Username: reviewer_pxd044996@ebi.ac.uk, Password: WeoaQaik); Project accession: PXD044993 (Username: reviewer_pxd044993@ebi.ac.uk, Password: 9wBe0DUA).

All proteomic data are under source data for each figure.

Research involving human participants, their data, or biological material

Policy information about studies with human participants or human data. See also policy information about sex, gender (identity/presentation), and sexual orientation and race, ethnicity and racism.				
Reporting on sex and gender	not applicable			
Reporting on race, ethnicity, or other socially relevant	not applicable			

groupings Population characteristics

not applicable

Recruitment

Blinding

not applicable

Ethics oversight

not applicable

Note that full information on the approval of the study protocol must also be provided in the manuscript.

Field-specific reporting

Please select the one below that is the best fit for y	your research. If you are not sure,	read the appropriate sections before	e making your selection

Ecological, evolutionary & environmental sciences

For a reference copy of the document with all sections, see nature.com/documents/nr-reporting-summary-flat.pdf

Behavioural & social sciences

Life sciences study design

All studies must disclose on these points even when the disclosure is negative.

Sample size Sample sizes were determined based on results obtained in previous proteomic and immunohistochemical studies on brain vessels published by the authors (e.g. see Zellner et al. Acta Neuroptahologica 2018; Beaufort et al. Proc Natl. Acad Sci 2014).

Data exclusions For the APOE-KO vs WT human iEC proteomic analysis n=1 APOE-KO sample was excluded because of incomplete APOE deficiency.

Replication
Animal-based experiments included over 4 independent animals per genotype, except proteomic analysis of BECs from AAV-treated mice which was performed on 4 independent BEC isolates derived from 2 mice per group. Replication of experiments was always sucessful.

Randomization Mice were randomly selected after genotyping. There was no experimental intervention that would have required randomization. Vessel lysates for immunoblot analysis were randomly selected.

Blinding was applied to immunohistochemical image analysis. For all other experiments, blinding was not possible in order to maintain the

homogeneity of the measurements (tissue processing and sample analysis were conducted alternately from the samples of the different experimental groups, avoiding batch effect and reducing technical variance).

Reporting for specific materials, systems and methods

We require information from authors about some types of materials, experimental systems and methods used in many studies. Here, indicate whether each material, system or method listed is relevant to your study. If you are not sure if a list item applies to your research, read the appropriate section before selecting a response.

Materials & experimental systems	Methods		
n/a Involved in the study	n/a Involved in the study		
Antibodies	ChIP-seq		
Eukaryotic cell lines	Flow cytometry		
Palaeontology and archaeology	MRI-based neuroimaging		
Animals and other organisms	•		
Clinical data			
Dual use research of concern			
Plants			

Antibodies

Antibodies used

Anti-Col4 Ab (Southern Biotech 1340-01); ICC dilution 1:400

Anti- Arf6 Ab (Invitrogen PA1-093); ICC dilution 1:200; WB dilution 1:250

Ant-Tfrc Ab (Invitrogen 13-6800) ICC dilution 1:200; WB dilution 1:250

Anti-Cldn5 Ab (Thermo Fisher 352588) ICC dilution 1:150 Anti-Pecam1 Ab (Abcam ab215911) ICC dilution 1:150

Anti-Cdh5 Ab (R&D systems AF938) ICC dilution 1:200

Anti-Apoe Ab (Santa Cruz sc-393302) WB dilution 1:500

Anti-Mbp Ab (Millipore MAB386) IHC dilution1:200

Anti-SSEA4 Ab (Abcam ab16287) ICC dilution 1:500

Anti-NANOG Ab (Cell Signaling 4903) ICC dilution 1:500

Anti-Tra160 Ab (Millipore MAB4360) ICC dilution 1:500 Anti-Oct4 Ab (Stemgent 09-0023) ICC dilution 1:500

Anti-Pecam1 Ab (R&D System AF3628) IHC dilution 1:100

Anti-NeuN Ab (Abcam ab104225) IHC dilution 1:200

Anti-Alexa-488 (Jackson Laboratories 715-546-150) ICC/IHC dilution 1:500

Anti-Alexa-488 (Jackson Laboratories 711-545-152) ICC/IHC dilution 1:500

Anti-Alexa-488 (Jackson Laboratories 705-546-147) ICC/IHC dilution 1:500

Anti-Cy3 (Jackson Laboratories 715-165-150) ICC/IHC dilution 1:500

Anti-Cy3 (Jackson Laboratories 713-103-130) ICC/IHC dilution 1:500

Anti-Cy3 (Jackson Laboratories 705-165-147) ICC/IHC dilution 1:500

Anti-Alexa-647 (Jackson Laboratories 715-606-150) ICC/IHC dilution 1:500

Anti-Alexa-647 (Jackson Laboratories 711-606-152) ICC/IHC dilution 1:500

Anti-Alexa-647 (Jackson Laboratories 705-606-147) ICC/IHC dilution 1:500

Goat Anti-Mouse Immunoglobulins/HRP (Dako; #P0447) WB: 1:10000 Goat Anti-Rabbit Immunoglobulins/HRP Dako; #F026102-2) WB: 1:10000

Validation

All Abs are commercially available and were used according to the manufacturer's instructions. Antibodies were validated by using only primary or secondary antibodies.

Eukaryotic cell lines

Policy information about <u>cell lines and Sex and Gender in Research</u>

Cell line source(s)

A18944: purchased from Thermofisher (Cat No: A18945); HEK 293 T cells: ATCC (Cat No CRL-3216)

Authentication A189044 Authenticated by manufacturer by flow cytometry (pluripotency), karyotype, pathogen test (for HIV-1, HIV-2, HTLV

type I and II, HSV-1, HSV-2, CMV, EBV, HBV, HCV) and mycoplasma by qPCR.

Mycoplasma contamination The line was regularly tested and confirmed negative for mycoplasma contamination.

Commonly misidentified lines (See ICLAC register)

Not commonly misidentified lines were used

Animals and other research organisms

Policy information about <u>studies involving animals</u>; <u>ARRIVE guidelines</u> recommended for reporting animal research, and <u>Sex and Gender in Research</u>

Laboratory animals

Mus musculus, mixed males and females, C57BL/6J (3,6,12 and 18 months old), APOE-KO (3 months old), ARF6-KO (3 months old), ARF6-GFP-AAV or GFP-AAV treated C57BL/6J mice (3 months old).

Animals were kept under standard conditions in a specific pathogen-free facility at 20-24°C and 45-65% humidity on a 12-h light/dark cycle and had access to food and water ad libitum.

Wild animals	The study did not involve wild animals.
Reporting on sex	Mouse-based analyses were performed on mixed gender experimental groups. The study was not designed for sex-based analyses and is not suitable for this purpose due to low sample size.
Field-collected samples	The study did not involve samples collected from the field.
Ethics oversight	Animal experiments were performed in accordance with the German Animal Welfare Law (§4 TschG) and approved by the Government of Upper Bavaria (Vet_02-21-139).

Note that full information on the approval of the study protocol must also be provided in the manuscript.

Plants

Seed stocks	not applicable
Novel plant genotypes	not applicable
Authentication	not applicable